Investigating the Fracture Behavior and Damage Mechanisms of Discontinuous Fiber Composites Under Significant Out-Of-Plane Loading

Kathryn Tidwell

A thesis
submitted in partial fulfillment of the
requirements for the degree of

Master of Science in Aeronautics & Astronautics

University of Washington

2020

Committee:

Marco Salviato, Chair

Jinkyu Yang

Program Authorized to Offer Degree:
William E. Boeing Department of Aeronautics and Astronautics

University of Washington

Abstract

Investigating the Fracture Behavior and Damage Mechanisms of Discontinuous Fiber Composites Under Significant Out-Of-Plane Loading

Kathryn Tidwell

Chair of the Supervisory Committee:
Assistant Professor Marco Salviato
Department of Aeronautics and Astronautics

This paper qualifies the interlaminar fracture behavior and damage mechanisms of discontinuous fiber composites. Laminates are produced by compression molding randomly distributed, pre-impregnated, unidirectional carbon fiber and epoxy platelets of size 50 mm by 8 mm with a thickness of 0.139 mm. Double cantilevered beam tests on geometrically-scaled specimens are completed, and qualitative and quantitative analysis is described in the following sections. Discontinuous fiber composites show complex damage progression in the form of fiber nesting, fiber bridging, crack bifurcation, and fiber breaking. This is visualized with digital microscopy, photographs during and after the test, and CT-scans that display internal damage. It is shown that the apparent fracture energy is size dependent, with the average interlaminar fracture energy increasing with the size of the coupon from approximately 0.54 N/mm to 0.80 N/mm. These values exceed reported inter-laminar fracture energy of traditional laminated composites by up to 167%. This is a result of complex damage mechanisms and tortuous morphology of the crack

TABLE OF CONTENTS

Page

LIST OF FIGURES

LIST OF TABLES

ACKNOWLEDGMENTS

I would like to acknowledge Professor Salviato for his guidance throughout this project, depth of knowledge and intuition for material behavior. I would also like to thank my mentor and fellow researcher, Seunghyun Ko, for being patient, knowledgeable, and supportive.

Chapter 1

INTRODUCTION

Composite materials are becoming more prevalent in fields including aerospace, automotive, maritime, and energy, [1]. This is in part due to their design-ability, high strength to weight ratios, and fatigue and corrosion resistance [2, 3]. They are conducive to larger more integrated methods that enable new design possibilities, larger assemblies, and a significant reduction in manufacturing and tooling [2]. Recently increasing in popularity, discontinuous fiber composites (DFCs) are manufactured from small randomly oriented platelets that provide material properties differing from standard composite laminates.

1.1 Description of Discontinuous Fiber Composites

DFC is comprised of randomly orientated rectangular platelets of unidirectional carbon fiber-reinforced pre-impregnetated fibers, shown in Figure 1.1, modified from [4]. Platelet size can vary based on manufacturer and design requirements. For this research platelets measure 50 mm by 8 mm and 0.139 mm in thickness. The random distribution of the platelets produce an orthotropic material. This is stacked, similar to a tradition layup, to create thicker laminates in a mat-stacking process [5, 6] shown in Figure 1.1, modified from [5]. DFCs are conventionally used in compression molding applications to create parts with complex three dimensional geometries.

1.2 Benefits of Discontinuous Fiber Composites

Discontinuous fiber composites are advantageous in modern design for a number of reasons including specific strength, reactivity, drapability, manufacturing methodology, out of plane properties, damage tolerance, and recyclability, [7–12]. Not dissimilar to traditional composite laminates, their high specific strength make them an ideal material for optimizing aircraft structures. With the increasing use of composites for primary aircraft structures

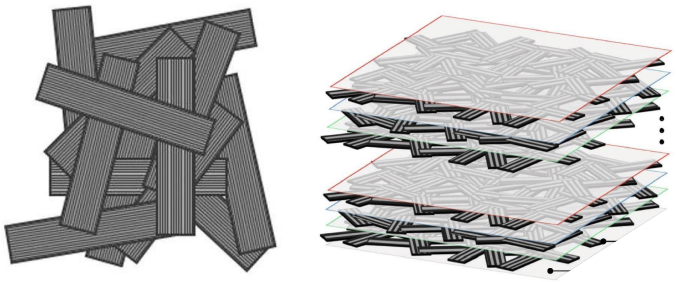

Figure 1.1: *Left*: discontinuous fiber composite made of platelets, [4] *right*: mat-stacking, [5]

comes complications at interfaces with secondary metallic structures. Carbon fibers are electrically conductive and elechrochemically noble. When metallic parts, manufactured from steel or aluminum, are connected to carbon fiber composites they become more susceptible to galvanic corrosion [7]. This incompatibility can be mitigated by adding external fiberglass plies to the carbon fiber composite part, or eliminated by replacing metallic secondary structures with composite parts.

Traditionally, if these secondary and tertiary parts are manufactured with carbon fiber, they are made with woven or stitched dry fabric and an infusion process. Smaller parts are often more complex in shape, so maintaining consistent flow in and around tight corners poses a considerable challenge. Variable flow results in resin rich or resin poor areas, which significantly decrease the strength and lifetime of a part. Moreover, unidirectional and woven fabrics are unable to effectively lay over and fill the complex geometries commonly present in secondary structures. Utilizing preimpregnated DFCs eliminates the low-flow molding conditions and produces a more consistent part. Instead of an infusion process, thermoplastic and thermoset DFCs are commonly manufactured with compression molding. The short length of the fibers in DFC make it ideal for forming into tight corners and over small radii. Not only does this increase the homogeneity of the part, it also substantially speeds production. Additionally, it is very common for secondary parts to experience load cases that contain out-of-plane components. The complex internal architecture of platelets in DFCs, lead to fibers oriented both in-plane and out-of-plane. This makes the part better

suited for three dimensional loading.

Another advantageous characteristic of DFCs, to be further investigated in this research, is their fracture energy. Research has shown that the intra-laminar fracture energy, which is a function of laminate thickness and platelet geometry, is approximately 5 times greater than that of aluminum, [11, 12]. This promotes and increase in damage tolerance.

Given the high cost and environmental considerations, recycling of carbon fiber composites has become increasingly important. The manufacturing of large scale composite parts produces a considerable amount of scrap material that is traditionally discarded [8]. It is estimated that there is 13 million kg of uncured scrap of carbon fiber prepreg dumped annually in the US, [9]. This is largely a product of ply cutter trim waste and out-of-spec material, [9]. This cast off uncured prepreg can be chopped into small platelets and re-purposed for compression molded discontinuous fiber parts. This eliminates some of the financial burden associated with disposing of uncured resins and large volumes of carbon. It is for all of these, and many other, reasons that discontinuous fiber composites are implemented in innovative designs today.

1.3 Current Uses in Industry

In the aerospace industry, any amount of weight savings contributes to fuel savings. To this effect, numerous metallic parts, traditionally made from steel, titanium, or aluminum, are being replaced with composite alternatives. The complex three dimensional morphology of secondary parts make DFCs an ideal fit. On Boeing's state of the art 787 Deamliner, the window frames are manufactured from Hexcel's HexMC. HexMC is a DFC prepreg manufactured by Hexcel with precision cut prepreg unidirectional tapes. It was chosen for its structural properties, net shape molding, improved fatigue, lower weight and corrosion resistance. This design saved nearly 50% in weight and offers superior damage tolerance, [13]. The Airbus A350 also sports parts manufactured from HexMC. This includes the fuselage crutches on A350-1000 [14].

It is not only metallic parts that are being replaced by DFCs. The access panel on the V-22 Osprey, a US Military Aircraft, was historically designed as a cored sandwich panel produced with woven carbon/epoxy prepreg and laid up by hand. The panel is roughly 16

inches by 14 inches and 0.5 inch thick [15]. Even though the part is relatively small, the time and money it took to manufacture it were appreciable. The panel was overhauled and is now compression molded out of Toray MS-4H. Manufacturing time is a fraction of what it used to be, taking only a matter of minutes to generate a new panel [15]. The material used, MS-4H, is a high-performance aerospace grade carbon/epoxy bulk molding compound that was developed by TenCate. It is a discontinuous fiber composite chopped from unidirectional carbon/epoxy prepreg, not dissimilar to the DFC manufactured for this research.

Lamborghini manufactures of number of parts out of DFC, or what they refer to as Forged Composites [16]. They boast that this material allows for integrated geometries, maximum flexibility, and molding cycles that are just 3 minutes long. In their manufacturing process, Figure 1.2, [16], dry fibers are chopped before the resin is added to create a pre-impregnated roll of DFC. This is then layered in a combined mold made from high quality steel that provides an ideal surface finish. Multi-axis pressure and localized distributed heating easily shape the part and allow for built-in reinforcements as well as variation in section thickness without the need to laminate additional materials [16].

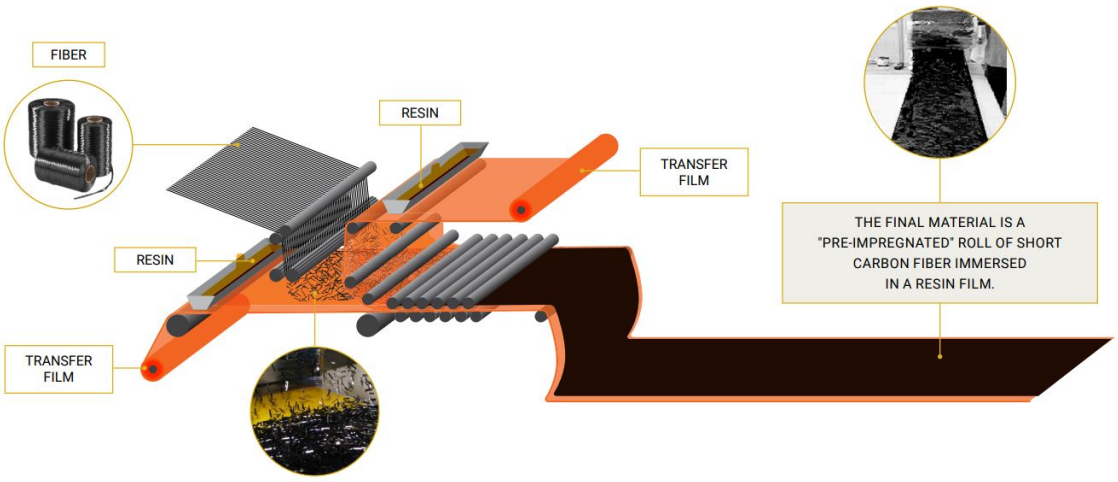

Figure 1.2: Manufacturing process of forged composites, [16]

Forged Composite technology was initially introduced on the inner monocoque and the wishbone suspension arms of the Sesto Elemento by Feraboli *et. al*, see Figure 1.3, [17].

Research and development of new parts had been focused on out of autoclave processes that could improve manufacturing efficiency. This, combined with the weight saving properties of composites and the three dimensional capabilities of DFC, motivated the design for these parts.

Figure 1.3: Inner monocoque and wishbone suspension arms, [17]

Now, Forged Composites are utilized not only for their structural capabilities, but also for their aesthetic design. The 2015 Huracan sports a Forged Composite engine bay cover and a stylish interior trim package that includes handles, air intakes, central tunnel cladding, and other details of the cockpit, [18, 19].

Figure 1.4: Lamborghini forged composite parts, [18,19]

In collaboration with Lamborghini, the golf company, Callaway, released a set of drivers

made out of Forged Composites called the Diablo Octane Drivers. DFC is one third the density of titanium, resulting in significant weight savings. Callaway claims that this clubhead has a greater transfer of power at impact and more accurate trajectories compared to traditional all-titanium clubs. This is accomplished by precisely setting the clubhead's center of gravity and moment of inertia through shape and thickness of the crown of the driver. Figure 1.5 shows a comparison between the old design of octane driver that uses a traditional composite fabric, and the new Diablo Octane Driver formed with DFC. With the use of compression molding, designs can be manufactured to a thousandth of an inch. The short fibers make it possible to more accurately fill the acute interior geometry. Notice the precise geometry of the DFC part compared to its predecessor. This club was so successful they released the Callaway RAZR Hawk and RAZR Hawk Tour Drivers, also craftily designed with Forged Composites [20, 21].

Figure 1.5: Octane driver with the old carbon fiber insides vs Diablo Octane with the Forged Composite technology, [20]

CRTC is a not-for-profit corporation in Port Angeles, Washington that focuses on the recycling of uncured carbon fiber composite into new customer products. Scrap material is received from Toray Composite Materials, and a number of other companies, and is repurposed into new customer products. These products include, a fully composite bench, Figure

1.6, that is immune to degradation from the elements like traditional wood benches, light weight pickle ball rackets and net, and even automotive seat backing. They have completed a significant amount of research into the manufacturing of discontinuous fiber composites. It is CRTC's mission to inspire and grow the global composite recycling community through innovation in technology and manufacturing that transforms carbon fiber scrap into products that positively impact people's lives and our environment.

Figure 1.6: CRTC Olympus Bench

1.4 Current Scientific Results Available

Designing with DFCs requires a comprehensive understanding of the interaction between complex internal mesostructure and material properties. In this pursuit, significant research to characterize and predict the behavior of this material has been completed. The properties of DFC are a function of many factors including fiber and platelet geometry, thickness of the laminate, architecture of the mesostructure, and distribution of the platelets. The majority of the research completed thus far to study the effect of these factors relates to tensile properties and elastic behavior. A number of studies have shown that the material properties of DFC are a function of platelet geometry [22–25]. Figure 1.7 shows a variety of platelet geometry studied by Kravchenko, [26]. Platelets measure in size of, from left to right: $\frac{1}{2}$" x

$\frac{1}{2}$", $\frac{1}{2}$" x $\frac{1}{8}$", $\frac{1}{2}$" x $\frac{1}{16}$", $\frac{1}{4}$" x $\frac{1}{4}$", and 1.2" x 0.4".

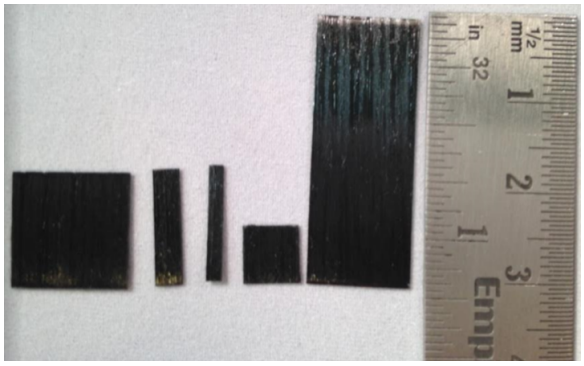

Figure 1.7: Various platelet geometries, [26]

Length-to-width and length-to-thickness of platelets appear to influence the tensile strength and modulus. Longer fibers also generate better tensile material properties [22, 24, 25, 27]. Increased interface connections between platelets better facilitate load transfer. However, Kravchenko *et al.* shows that there is a trade-off between variability and mechanical properties [24]. Increasing the platelet length can increase the variability of the tensile strength whereas, platelets of short length create a more uniform material and result in decreased variability and strength. Figure 1.8 shows the strength of a laminate as a function of platelet size, [26]. It is clear that increasing the size of the platelet results in larger tensile strength.

Material properties can also be manipulated by changing the size of the tow. Typically DFC have lesser but comparable stiffness and strength compared to an equivalent quasi-isotropic layup [5, 25]. Through numerical modeling and testing, Alves *et al.* shows that thin towed (about 20 microns) material makes it possible to match the strength of a quasi-isotropic continuous fiber laminate and surpass its stiffness [5]. This is due to the improved stress transfer between platelets. The thinner platelets increase the homogeneity of mechanical properties in comparison with traditional thicker towed laminates [5, 24, 25]. Figure 1.9 shows a comparison between a standard DFC, HexMC-M77, and a thin towed DFC, HM-20-1600, [5]. Notice that the HecMC-M77 has a large amount of tape waviness, while the tape in HM-20-1600 lies relatively flat resulting in increased mechanical properties due to in-plane fiber alignment and through thickness homogeneity.

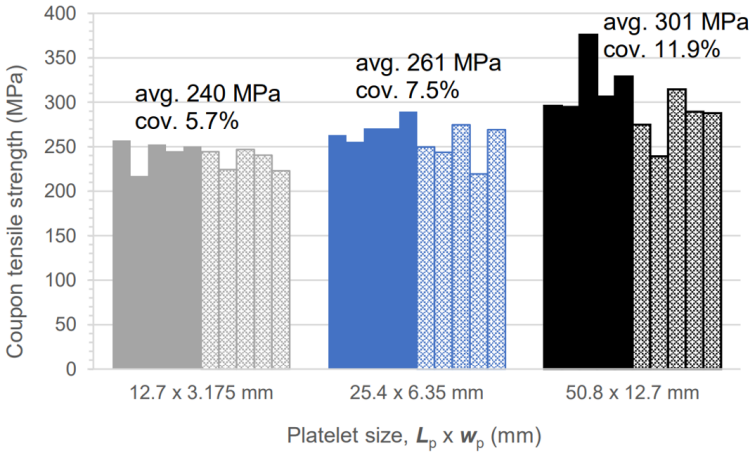

Figure 1.8: Platelet size vs effective tensile strength, [26]

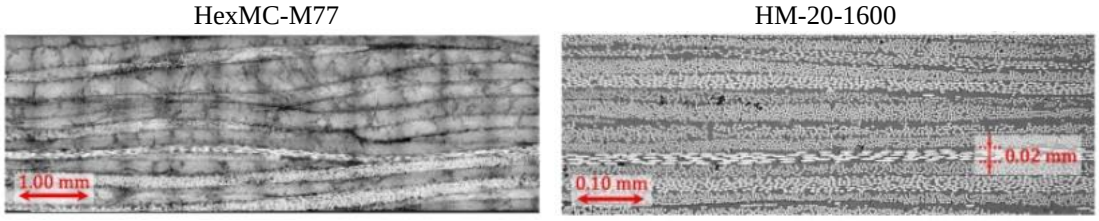

Figure 1.9: Micrographs of cross-sections of different material systems, [5]

Fiber orientation also contributes significantly to the material properties [24]. Platelets are markedly stronger in tension in the fiber direction, and this strength is propagated to the laminate properties. Aligning platelets with the loading direction improves the tensile stiffness and strength [24].

Additionally, increasing the overall thickness of the laminate reduces the variability of platelets through the thickness. This has a positive effect on the elastic tensile properties [22–24]. Outside of elastic properties, increasing the thickness of the laminate is also shown to have a positive effect on flexural properties [28], and intra-laminar fracture energy [11].

Yamamoto *et al.* uses three point bending tests to evaluate bending flexural strength and flexural modulus [28]. The results show that increasing thickness and width of specimen

decreases the variation on mechanical properties. The complex mesostructure and random placement of the platelets cause inconsistencies in material properties throughout the laminate. The non-uniform distribution of the number of platelets through the thickness results in stress concentrations, and resin rich areas which weaken the composite. Reducing these defects will significantly improve the material properties and decrease variation.

Ko *et al.* utilizes Single Edge Notch Tension Tests to analyze the fracture energy and the equivalent fracture process zone size as a function of the thickness of the laminate [11]. The fracture energy is shown to increase with the thickness of the specimen and level off at a thickness of 3 mm. The fracture energy is calculated to be 57.77N/mm, which is approximately 4.81 times larger than that of aluminum. For sufficiently thin specimens, Ko *et al.* shows that fracture can initiate from weaker sections of the laminate instead of at the notch. He presents the notch sensitivity as a function of laminate thickness, and notes that the thicker the specimen the less likely the crack will originate away from the stress-free notch. When a part is sufficiently thin there are not adequate distribution of platelets to uniformly distribute the load. This results in stress concentrations away from the notch.

Ko *et al.* also demonstrates that fracture energy is dependent on platelet size [12]. His research in intra-laminar size effect of DFCs reveals that platelets of 75x12 mm have a 96.8% increase in fracture energy compared to platelets of size 25x4 mm. Moreover, he establishes that the effective fracture process zone length increases with platelet size, leading to the laminates of smaller platelet size exhibiting increased brittleness.

In all of the research and computational models that have been developed, the inter-laminar fracture energy has been largely overlooked. There is a preliminary study done by Guo *et al.* that examines Mode I fracture in DFC, [29]. Unstable crack growth was visualized, the fracture energy was computed by implementing a number of different methods, and numerical solution was created that shows good correlation to experimental results. In calculating the fracture energy, Guo *et al.* employs modified compliance calibration (MCC), modified beam theory (MBT) and beam theory in reference to JIS K 7086 standard.

These theories were derived from a simple beam models, which are insufficient to capture the extreme non-linearity of the crack front. It is assumed that each “beam” or top and bottom side of the specimen has a constant elastic modulus. The complicated mesostructure

of DFC laminate generates a non-negligible waviness though the midplane of the laminate. This waviness causes a change in thickness of the beams which results in a variable elastic modulus. Additionally, these methods require the length of the crack during fracture, which is nearly impossible to accurately determine. Given the exceptionally quasi-brittle nature of DFC, shown by Ko *et al* [11, 12] the fracture process zone, although not visible, is definitely non-negligible. Energy dissipated in micro damage ahead of the crack front will artificially raise the fracture energy, yielding inaccurate results.

In order to create a numerical model or failure criteria that can accurately describe the failure mechanism and physics of delamination of DFC, it is critical to be able to visualize the crack front and propagation. Recent studies have been completed utilizing CT scans to visualize internal damage.

Kravchenko *et al.* uses CT-scans to determine the platelet orientation [24]. This data is then explicitly loaded into the computational model to match the mesostructure of the coupon. Integrating this information into the simulation more accurately depicts the material behavior and allows for prediction of the various stress concentrations and damage areas. CT- scans were also used to visualize internal damage of tensile specimens post failure. Figure 1.10 shows the minimum amount of surface damage compared to the extensive internal damage that exists beneath the surface [24].

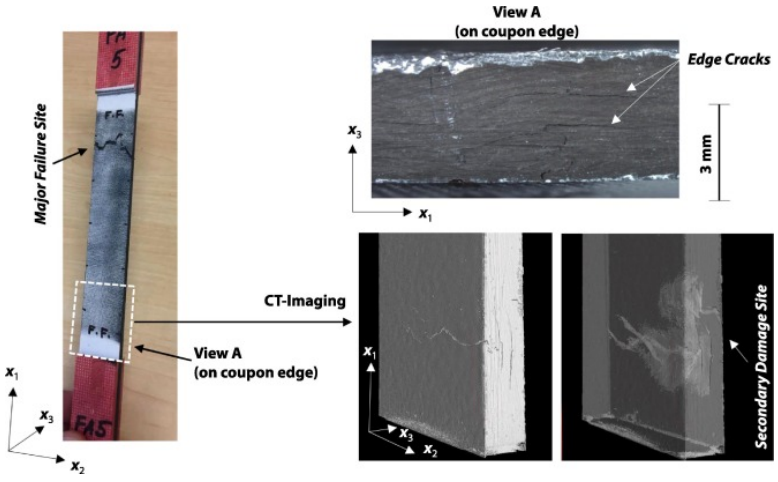

Figure 1.10: Results after tension test, [24]

Chai *et al.* presents 3D images of damage evolution in woven composite tubes under torsion taken with a CT-scanner [30], which enabled characterization of damage modes and their damage sequences. Figure 1.11 depicts the distinct types of damage and indicates when during loading they occur [30]. Understanding the complex sequence of damage propagation is critical for the safety of design. This cutting edge imagery can provide insight into the magnitude of the non-visible internal damage, and advance the understanding of material failure.

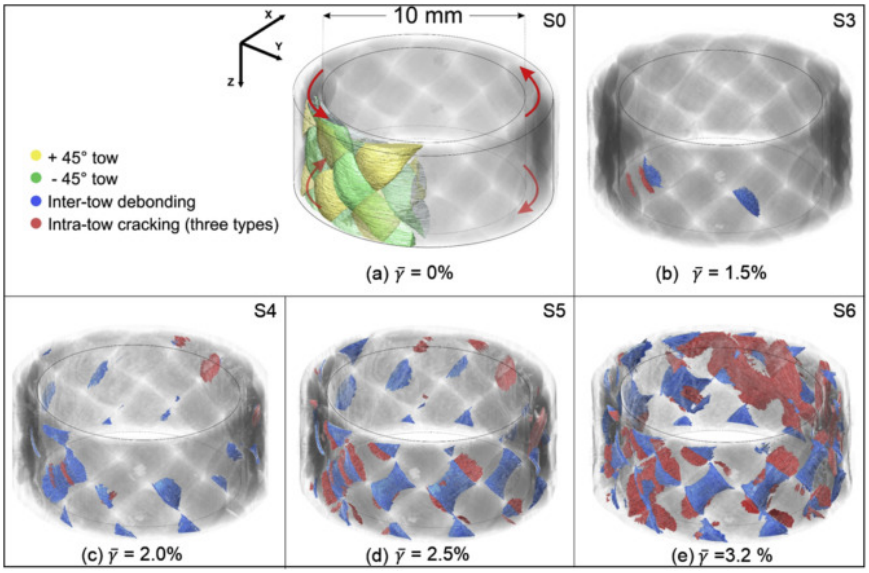

Figure 1.11: Damage initiation and propagation, [30]

Kravchenko *et al.* did a study to evaluate the effectiveness of a DFC part experiencing out-of-plane loading on the part seen in Figure 1.12, [26]. The compression molded part was manufactured from chopped prepreg of continuous unidirectional fibers. The platelet size, initial material charge state and manufacturing methodology of pinhole were varied. Two processes for creating the pin holes were applied; molded-in and drilled. The molded-in pin hole parts have a knit line that formed due to the flow dividing around the pin hole and the two flow fronts meeting again on the other side. A CT-scan clearly depicts the knit line in Figure 1.13, [26].

Figure 1.12: Compression molded part, [26]

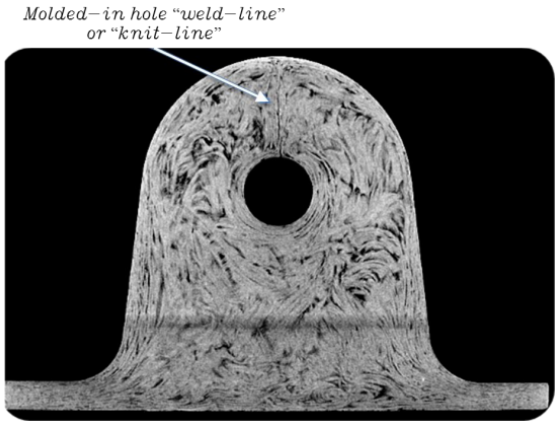

Figure 1.13: CT scan with knit line on compression molded part, [26]

The molded-in pin hole parts primarily failed at the knit line. Following the damage progression, secondary failures also occasionally occurred in the base due to bending, Figure 1.14, [26]. Conversely, the drilled-in pinhole parts did not have a knit line and as such did not experience failure at the top of the part. Failures were generally localized to the base/flange junction. Visualization of these failures and their corresponding load and displacement

curves are shown in Figure 1.14, [26]. Notice the jagged morphology of the cracks present in both parts. Kravchenko et al. notes that in these tests, the damage develops long before ultimate failure. Unlike a traditional delamination, which can propagate unstably and unimpeded, the DFC part experiences damage locally and the stress redistributes to the surrounding platelets so that the system can maintain the load [26]. The architecture of traditional laminates does not support this load re-distribution. Out-of-plane loads are primarily limited to the interlaminar tensile strength of the laminate, which is exceptionally small in comparison. This principal observation gives significant incentive for continued study and design of DFC.

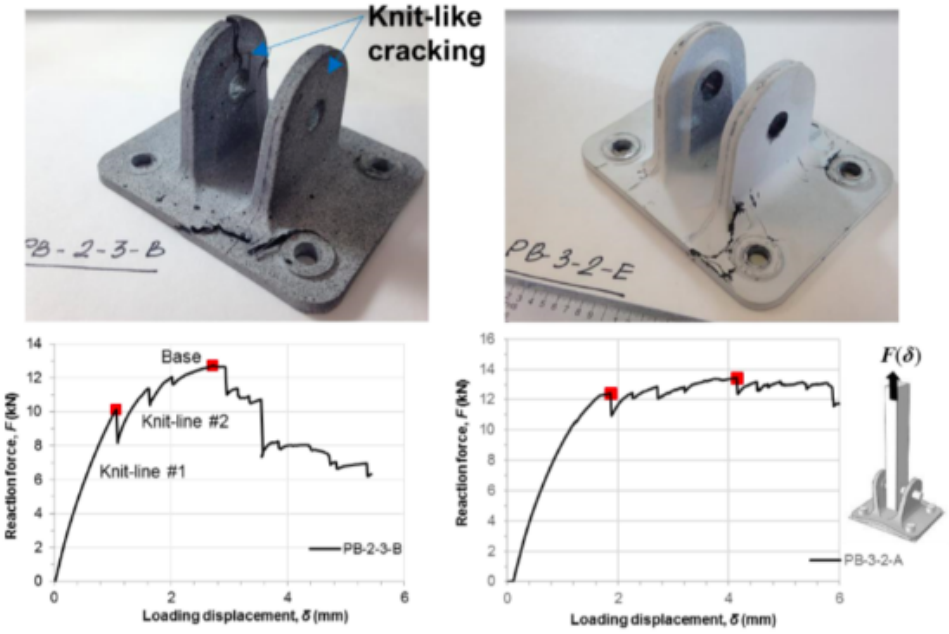

Figure 1.14: Failure in pin-bracket parts, *left*: molded-in pin holes *right*: drill-in pin holes, [26]

1.5 Motivation

As mentioned previously, companies are starting to rely on composites for secondary parts, many of which experience out-of-plane loading conditions. This loading condition is notoriously hazardous for traditional laminates due to their tenancy to delaminate. This is one of

the primary failure mechanisms, and occurs when two adjacent plies are separated causing loss of stiffness and deterioration in performance. There are three classifications of fractures that are traditionally considered: Mode I, Mode II, and Mode III, the opening, sliding, and tearing mode respectively, see Figure 1.15. Mode I typically has the lowest fracture energy, and as such is generally regarded as the most critical. For that reason, this research focuses on double cantilever beam tests to assess the resistance to delamination. Once a laminate begins to delaminate, the crack is very easily propagated and the damage can spread exceedingly fast. The complex mesostructure of DFC parts make them better suited to handle three dimension load cases.

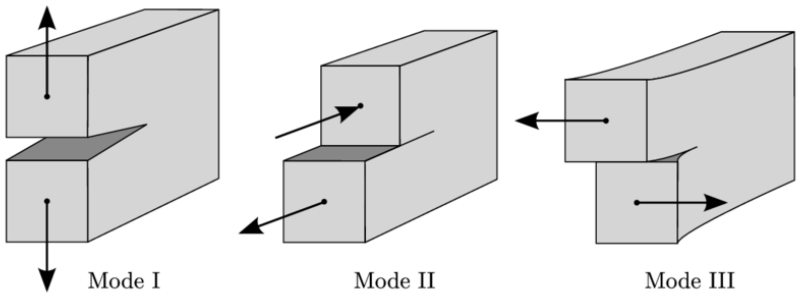

Figure 1.15: Modes of fracture

The image on the left in Figure 1.16 shows a curved beam strength specimen utilized by Yavuz *et al.* to determine inter-laminar tensile strength of a unidirectional composite laminate [31] . Notice the delamination between plies originating at the corner of the specimen. Since each ply has a smooth interface with adjacent plies, the crack propagates unimpeded. In comparison, the image on the right of Figure 1.16, is constructed from DFCs. The cracks are jagged and propagate through multiple planes, suggesting increased fracture energy.

The measure of this resistance is the inter-laminar fracture energy and can be determined by several different analytical approaches. For isotropic materials, such as metals, Linear Elastic Fracture mechanics or Elastic Plastic Fracture mechanics is widely accepted and utilized. Unfortunately, due to the orthotropic material properties of composites, the complex mesostructure of discontinuous fibers and strong quasi brittle behavior, this method fails

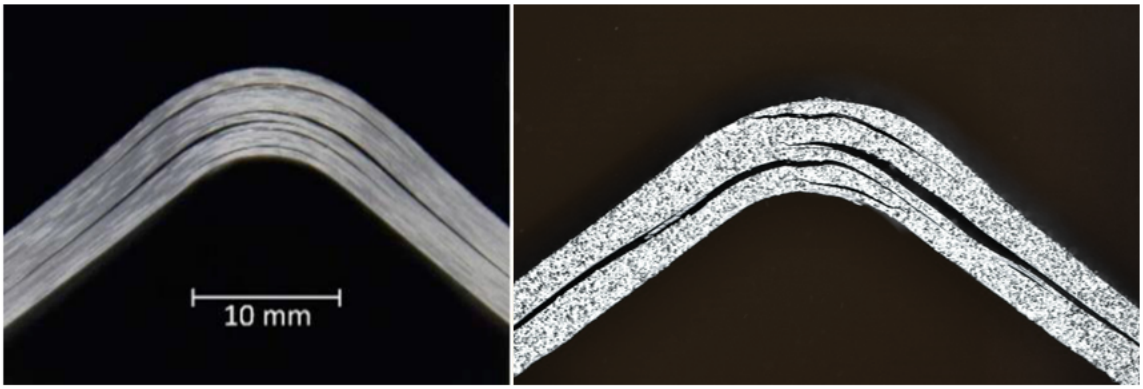

Figure 1.16: Curved beam strength specimen, *left*: unidirectional laminate, [31] *right*: DFC laminate

to capture the energy dissipated during fracture. The goal of this paper is to describe the failure mechanisms that occur in during inter-laminar crack propagation and comment on the beneficial results of complex internal architecture.

Chapter 2

MATERIALS AND METHODS

2.1 Manufacturing Process

The fabrication of DFC in this study follows the in-house manufacturing process developed by Ko [32] *et. al.* This process was used to ensure full control of platelet size and laminate thickness. Purchasing a product like HexMC, Hexcel's discontinuous fiber prepreg, forfeits the ability to minutely control laminate properties. Additionally, manufacturing the product in house facilitates a full understanding of micro and mesostructure of the material.

The DFC was manufactured from Toray T700G-12K, 150 gsm with 35% resin content. Prepreg rolls were cut on a CNC fabric cutter machine into combs 8 mm in width. These combs were separated and cut perpendicularly, producing 8 x 50 mm chips. The chips were randomly distributed into a 400 x 400 mm Teflon lined box to create 100 g square mats. These mats were stacked on top of each other until the desired laminate thickness is reached. The stack was periodically debulked during this layup to remove porosity. Debulk occurred every 300 g, or every three mats, and lasted for two hours under 100 psi. At the midplane of the layup, a piece of Teflon was inserted in order to create a precrack as designated by ASTM D5528-13. The laminate was then cured in a heated platen press per manufacturing standards. The ramping cycle was the following: 4.5 ^{o}C/min up to 270^{o}C, hold 270 ^{o}C for two hours, and 9 ^{o}C/min cooling to the room temperature. Throughout the cycle, the applied force was held at 11.6 tons, see Figure 2.1. A tile saw was used to cut out coupons. Coupons were cut 1.5 inches from the edge of the laminate in order to avoid inconsistencies in laminate thickness, resin starved areas, and other defects. The manufacturing process is summarized in Figure 2.2.

The coupon size and test methodology follows that of the ASTM Standard D5528-13: Standard Test Method for Mode I Interlaminar Fracture Toughness of Unidirectional Fiber-Reinforced Polymer Matrix Composites. Piano hinges were cut at 45 mm to match the width

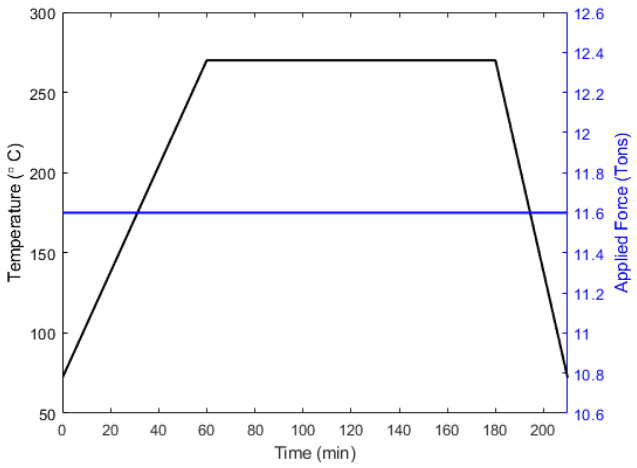

Figure 2.1: Cure cycle in heated platen press

of the widest specimen. Hinge and coupon surfaces were scrubbed with 80 grit sandpaper and thoroughly cleaned with acetone to remove dust and oil to promote quality bonding. Hinges were bonded to the end of the specimens with JB Weld and allowed to set completely. The precrack was made along the length of the teflon insert. Clamps were used to ensure that precrack did not exceed the desired length. Finally, hinges were secured with a centrally located nut and bolt to assure load transfer without debonding. Specimen preparation is depicted in Figure 2.3.

2.2 Specimen Sizing

It has been shown that composite materials do not follow traditional plasticity or Linear Elastic Fracture Mechanics [33–44]. This is due to the non-negligible size of the fracture process zone (FPZ), where mico-damage occurs in front of the stress free crack. Traditional methods of calculating the fracture energy require a precise location of the crack tip. This becomes increasingly difficult with the non uniformity of the crack front and the large size of the FPZ exhibited in DFC. The Mode I fracture energy can be more accurately captured using Bazant's Type II Size Effect Law [45]. The size effect method of testing only requires the peak load obtained during the test and eliminates the error in approximating the location

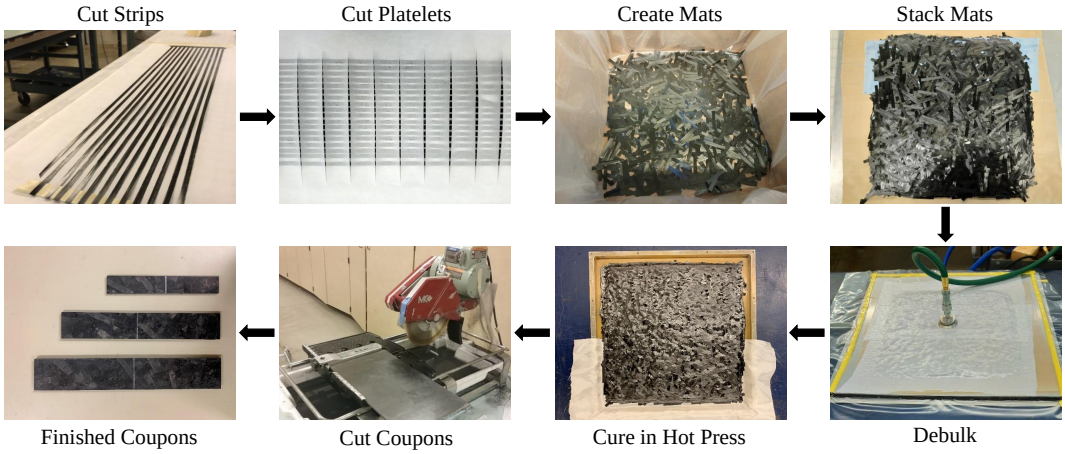

Figure 2.2: Manufacturing of coupons

of the crack front. To this effect, three sizes of coupons were manufactured.

ASTM Standard D5528-13 requires that double cantilever beam specimens be of a minimum size of 125 mm long and nominally from 20 to 25 mm wide, with the initial delamination length of approximately 50 mm. The laminate thickness should nominally be between 3 and 5 mm. These parameters were observed to shape the first size specimen. From there, the specimen was scaled up in size in three dimensions with ratio 1:1.5:1.8. Coupon dimensions are presented in Table 2.1 and Figure 2.4

Size	Delamination Length $a_0(mm)$	Length L (mm)	Thickness t (mm)	Width w (mm)	Scaling Ratio
1	50	128.5	3.17	24.91	1
2	75	195	4.65	38.85	1.5
3	90	233.5	5.99	44.84	1.8

Table 2.1: Specimen geometry

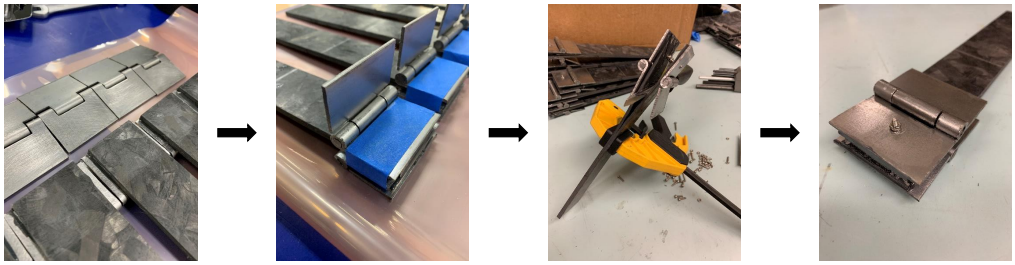

Figure 2.3: Attaching of hinges

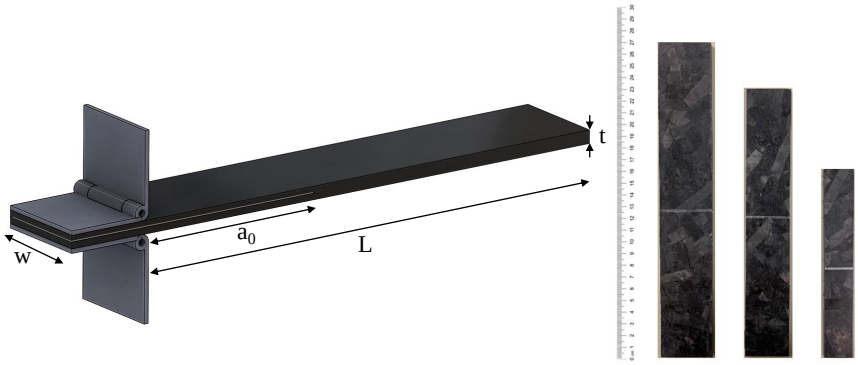

Figure 2.4: Specimen geometry

2.3 Double Cantilever Beam Test

The Double Cantilever Beam (DCB) tests were completed on an Instron 5585H load frame with a 1-10 kN load cell, as seen in Figure 2.5. The tests were completed under a displacement control of 3-5 mm/min per ASTM standard. The rate was adjusted for each size of coupon to maintain a consistent strain rate. Each test took approximately 10-15 minutes. Load, displacement, and time data was collected throughout the test and are presented in the following sections.

Figure 2.5: Test set up

Chapter 3

MORPHOLOGICAL CHARACTERIZATION OF DAMAGE MECHANISMS

This section will focus on the damage in DFC that occurs during fracture. Initially, damage is visualized in a microscopic scale where small amounts of damage occur on a fraction of a platelet. Then, damage mechanisms will be defined and characterized on a mesoscale. That is, the evolution of damage over an entire platelet or series of platelets. Finally, CT-scans are presented to give a macro-scale view of the crack front.

3.1 Micro Damage

On a microscopic scale, DFC experiences various types of localized damage. This includes matrix cracking, fiber breaking, fiber pull out, and delamination. All of which occur frequently in each size of specimen tested. This microdamage contributes to the energy required to propagates the crack through the material. In general, the stronger the material, the more energy required to break it. Composite failure can be decomposed into two classes; matrix failure and fiber failure. Given that the strength of fiber is much larger than that of the matrix, the fiber dominated failures require significantly more energy. To identify the microdamage that occurs during fracture, images were taken with an Omax 9 MP camera with Nikon M Plan 20 objective.

3.1.1 Delamination

Delamination results from cohesion failure between two plies. Figure 3.1 shows the surface of a portion of a platelet after it has delaminated from the adjacent platelet. Notice that the surface is relatively smooth and the fibers remain intact with their respective platelets. This is a matrix dominated failure mode and does not require significant energy to propagate the crack.

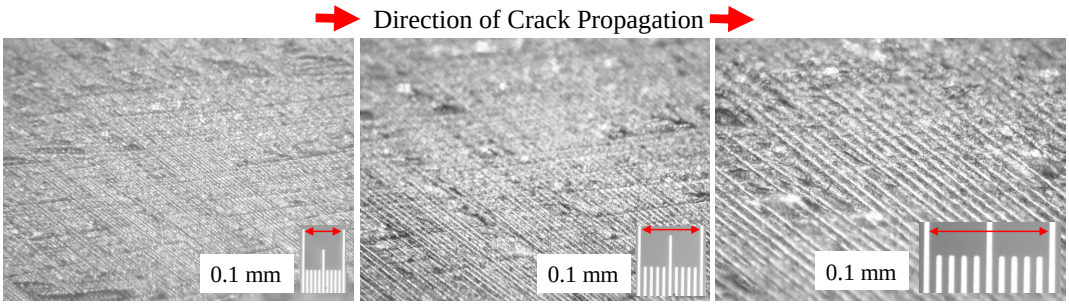

Figure 3.1: Delamination under optical microscope

3.1.2 Matrix Cracking and Deformation

Matrix cracking is a common occurrence in composite materials. In itself, matrix cracking does not always directly result in laminate failure. The primary function of the matrix is to transfer loads between fibers, which can be diminished by the presence of significant matrix cracking. However, the localized damage caused by matrix cracking does absorb energy improving the overall damage resistance. Sufficient micro damage ahead of the crack results in pseudo-plasticity. Matrix cracking is visualized through the optical microscope in Figure 3.2, highlighted by the red circle. The fibers go from the bottom right hand corner to the top left hand corner of the image and present as smooth straight lines. The matrix cracking is perpendicular to the fiber direction and cracks are jagged.

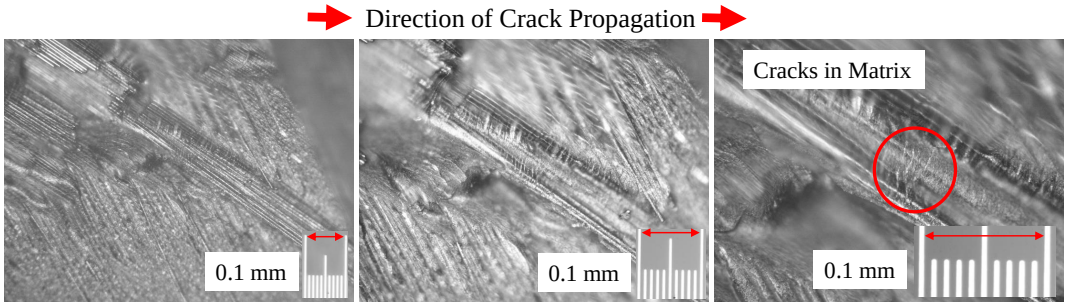

Figure 3.2: Matrix cracking under optical microscope

3.1.3 Fiber Breaking

In composites, the majority of the load is carried by the fibers. When this load exceeds the strength of the fibers, the fibers break. Often times, if one fiber breaks the matrix is able to transmit the load to the surrounding fibers, but this is not always the case. If the load is not adequately distributed, adjacent fibers will also break. Figure 3.3 shows clusters of fibers in a DFC coupon that have all broken as a result of stress concentrations during a DCB test. This is a fiber dominated failure mode that is not observed in DCB tests of a traditional laminate. Due to the high tensile strength of the fibers, this failure mode requires a large amount of energy compared to delamination. Since delamination is the primary mechanism for Mode I fracture in traditional laminates we can expect a higher fracture energy of DFC.

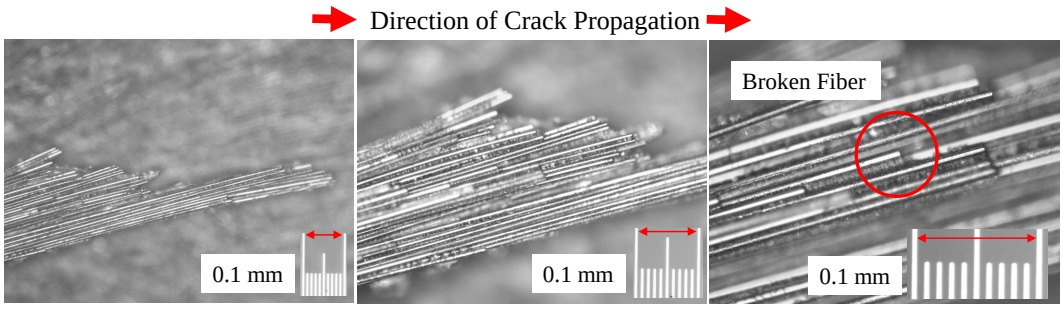

Figure 3.3: Fiber breaking under optical microscope

3.2 Damage Mechanisms

3.2.1 Delamination

As visualized on a microscopic scale, delamination occurs when two adjacent plies separate from one another as a result of interlaminar stresses that exist between each ply, Figure 3.4. Delamination on a mesoscale occurs over a series of platelets and is common during unstable crack propagation. It can lead to part failure, decreased mechanical properties, and shortened lifespan. In traditional laminates, the Mode I fracture energy is calculated as the resistance of delamination. In DFC, delamination represents only a fraction of the complex damage progression that occurs in Mode I fracture.

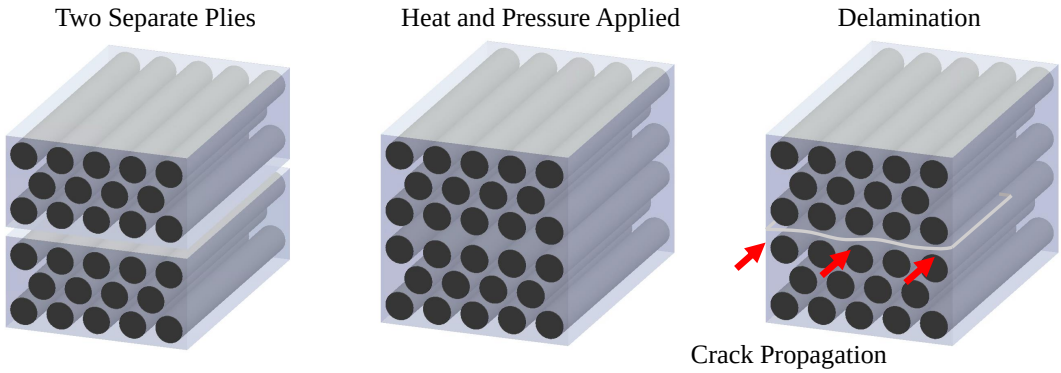

Figure 3.4: Delamination

3.2.2 Fiber Nesting

Fiber nesting is common in unidirectional laminates with fibers parallel to the direction of crack propagation. As shown in Figure 3.5, fibers migrate from one ply to another during the cure cycle. When this occurs, there is no clear path for delamination to propagate [46]. This can be caused by standard heat and pressure applied during cure as well as fibers aligning due to resin flow. In DFC, this occurs when two platelets are oriented in a similar direction and are parallel to the direction of crack propagation.

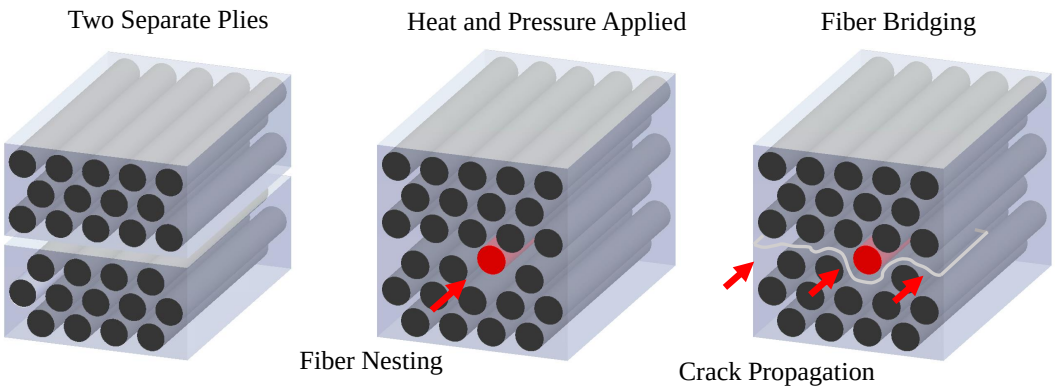

Figure 3.5: Fiber nesting and fiber bridging

3.2.3 Fiber Bridging

Fiber bridging is commonly a result of fiber nesting. The wandering crack causes the nested fiber to be split between both new crack surfaces [46]. Additionally, fiber bridging can be initiated through micro damage ahead of the crack front. Since DFC is a quasi-brittle material, it has a non-negligible fracture process zone (FPZ) ahead of the crack tip. The FPZ is an area in front of the crack tip containing extensive micro damage that subsequently leads to softening of the material. As shown in Figure 3.6, this micro damage can progress, forming a new crack and causing the fiber to bridge. This is also visible in Figure 3.7 of a specimen during test. The primary crack is visible and just ahead of it, a secondary crack on an adjacent plane, is beginning to form.

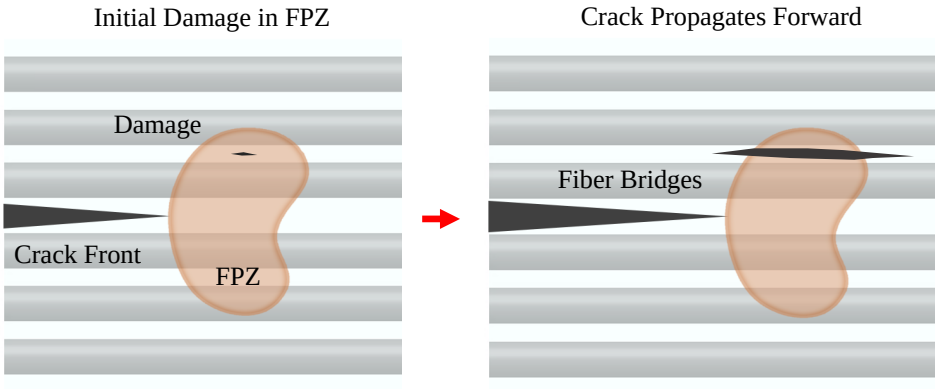

Figure 3.6: Fiber bridging

Figure 3.8 shows the presence of fiber bridging further along in the test. Fibers bridge across the two new crack surfaces demanding extra energy be applied to propagates the crack further. After testing is complete, the location of fiber bridging is exceedingly visible. Note that in both specimens in Figure 3.9, the fibers that have bridged are closely aligned to the direction of crack prorogation. Instead of delaminating between platelets the fiber bridging has forced the crack as split down the center of a platelet, leaving some of the fibers on each new surface. The macroscopic fracture energy can be considered to be the sum of the energy

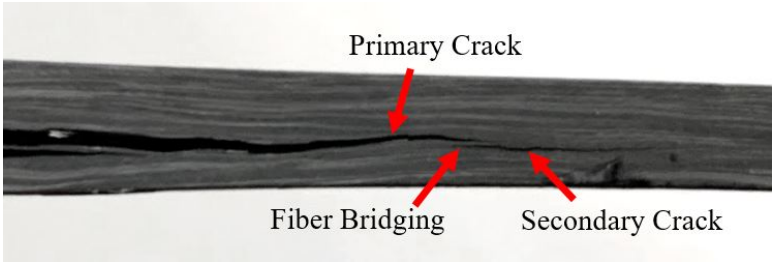

Figure 3.7: Side view of fiber bridging during DCB test

required to break a multitude of microscopic bonds along the crack surface. Consequently, the larger the surface area created by the crack, the larger the fracture energy required to create it. When a fiber bridges, it creates an increased amount of new surface compared to a fiber that remains intact with its respective platelet.

Figure 3.8: Fiber bridging during DCB test

3.2.4 Crack Bifurcation

Crack bifurcation occurs when the singular crack front splits and two or more cracks continue to propagate forward. This can occur as a result of inhomogeneities, microstructural discontinuity, and local stress state. Fibers transverse to the direction of crack propagation

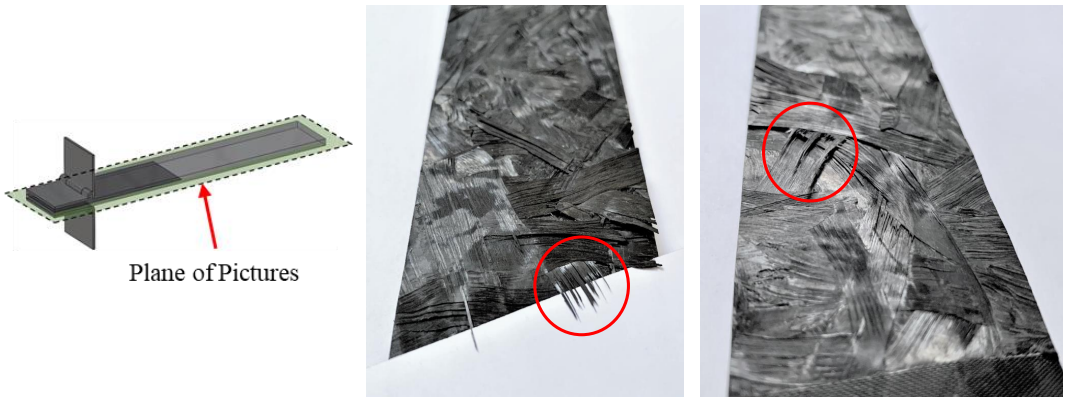

Figure 3.9: Fiber bridging on newly created surface after DCB test

have been demonstrated to deflect crack front away from coplanar fibers [47, 48]. This deviant crack tip behavior, as opposed to planar crack propagation, results in a mixed mode crack front behavior.

In Figure 3.10 shows multiple crack fronts as a result of crack bifurcation. The crack propagated with a single crack front until it reached a transverse platelet. At this point, the crack splits into two, navigating around the transverse platelet. It is important to note that this crack bifurcation occurs when the transverse fiber is at the edge of the coupon. This may be a result of contributions from edge effects. Further testing of wider specimens is required to validate this observation.

Given the nature of the DCB specimen, a visual inspection of the crack does not give sufficient detail of its complex geometry. To remedy this, a NSI X5000 micro-CT scanning system was used to take an internal image of the crack front. More information regarding CT-Scans and image processing are discussed in Section 3.2.6. Figure 3.11 shows a slice of the CT-Scanned volume. Two jagged cracks propagate through the specimen. Notice that the cracks are not in the same plane and do not propagate in a straight line. Conversely, a crack propagating through a unidirectional laminate is exceptionally smooth and grows uniformly through the midplane of the laminate, see Figure 3.11. The multiple irregular cracks through the DFC generate significantly more new surface area and consequently

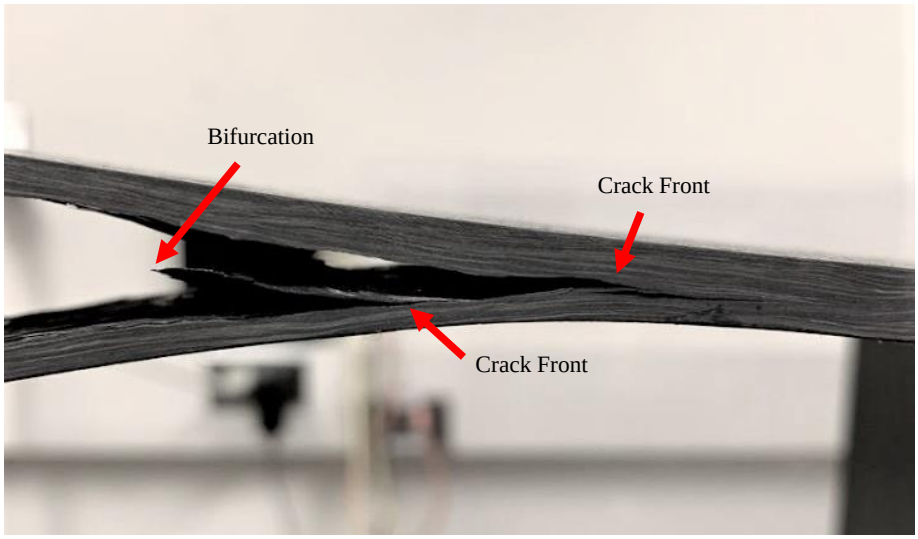

Figure 3.10: Crack bifurcation during DCB test

requires greater energy.

3.2.5 Damage Progression

There are a common patterns of damage present in the DCB tests. In reference to Figure 3.12, the picture on the left shows the entire new surface created as a result of propagating the crack through the entirety of the coupon. On the right, a piece of paper was slipped under the transverse platelet to visualize the magnitude of the double crack propagation before the crack front re-consolidated. The crack propagates from the bottom to the top of the picture. Initially visible, the feathered fibers present in direction of the crack propagation are indicative of fiber nesting and fiber bridging. From there, the crack encounters a platelet oriented transverse to the direction of propagation which causes a bifurcation to occur and the singular crack front to split into two. The behavior has been identified on a number of specimens tested and occurs when the transverse platelet has a free edge. This is shown in Figure 3.12.

Another common progression of damage is fiber nesting leading to fiber bridging, and

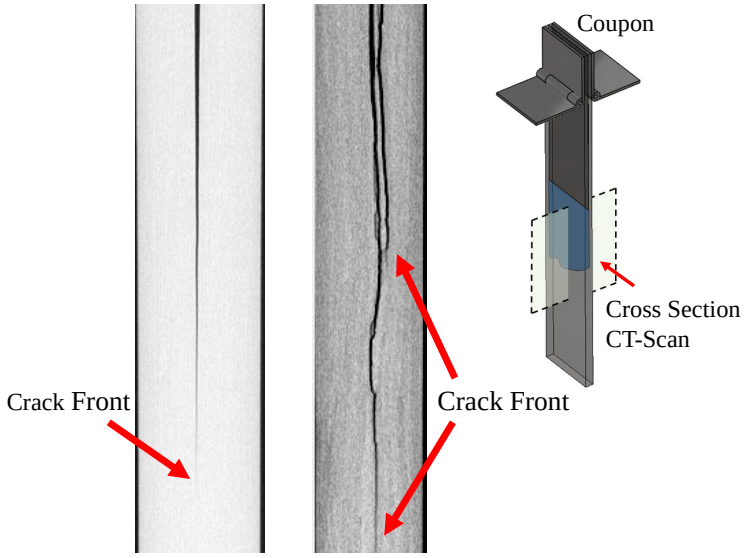

Figure 3.11: Internal crack visualization with CT-scan of *left:* unidirectional composite *right:* DFC with crack bifurcation

fiber breaking. Once the fiber bridges, the opening load is carried by the fiber in tension. When the load exceeds the strength of the fiber, the fiber breaks. This produces an audible 'ping' during tests.

Often times multiple types of damage mechanism occur simultaneously during fracture. Figure 3.13 demonstrates this combination of complex damage mechanisms. Single fibers, or small groups of fibers bridge between the two arms of the specimen. Some of these fibers have already broken in tension. Additionally, multiple crack fronts are present. A combination of all of these damage mechanism results in an increased energy require to break the specimen. In a traditional composite laminate, Mode I fracture results in pure delamination and creation of two new smooth surfaces. As discussed earlier, delamination requires a relatively low amount of energy because it is a matrix dominated failure mode. As is obvious from Figure 3.12, the jagged crack and out-of-plane crack propagation results in much larger surface area. Since fracture energy is a function of surface area generated, this suggests the fracture energy of DFC will be larger than that of a traditional laminate.

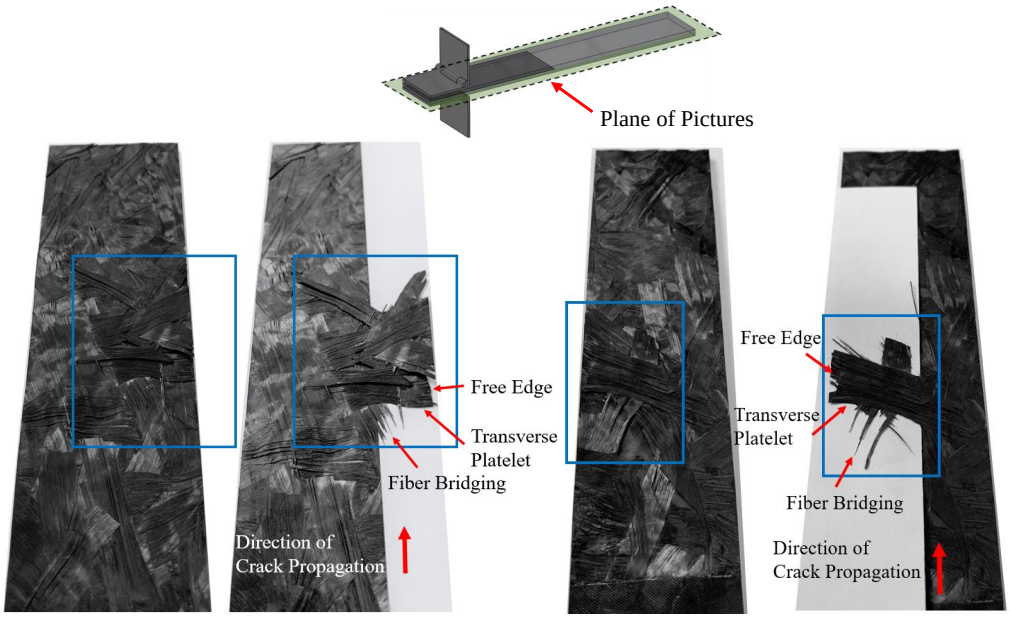

Figure 3.12: Damage progression on newly created surfaces after DCB test

3.2.6 CT Scanning

Due to the complicated internal mesostructure of DFC, traditional analysis and assumptions about crack front and damage do not apply. The geometry of a DCB specimen makes it exceedingly difficult to visualize the crack and newly generated surfaces during propagation. In order to understand the magnitude of non-visible internal damage, CT-scans of the crack fronts were taken. This method of visualization is nondestructive, and shows promise for damage identification in future parts. A NSI X5000 scanning system was used on a number of coupons to help visualize the crack front. The goal was to track the crack as is propagated through the specimen: take a CT-scan of the coupon before it was tested, after once the crack was propagated a small amount, and again after the crack was propagated a second time.

Some of the coupons were soaked in a dye penetrate to help illuminate the damage. The dye penetrate was a mixture of 250 g zinc oxide, 80 ml isopropyl alcohol, 1 ml Kodak

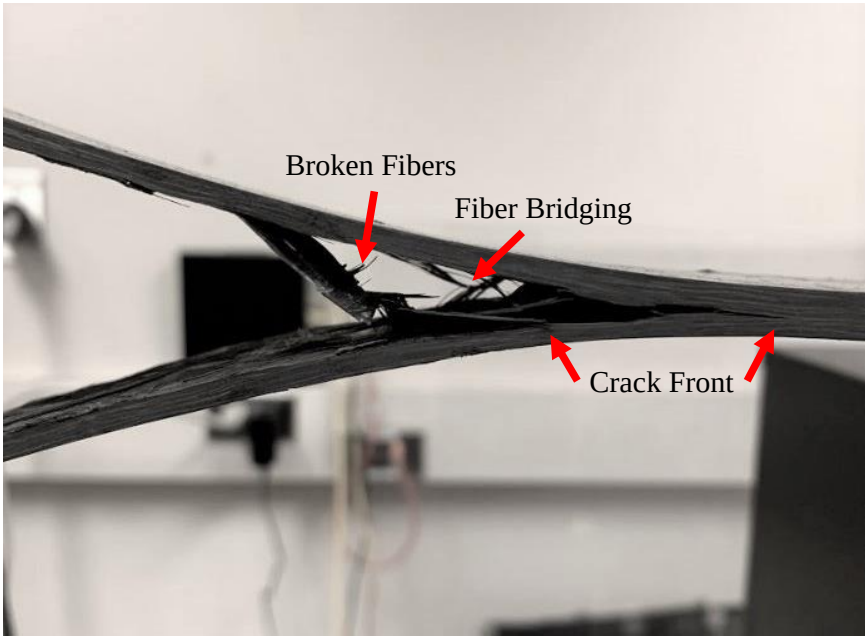

Figure 3.13: DFC specimen during DCB test

solution, and 80 ml distilled water. Coupons were soaked for 12 hours, then allowed to dry before scanning. The zinc settles into the cracks and damage that exist in the coupon. The difference in density between the composite, air, and zinc provide a clear image of the internal damage. Unfortunately, the dye penetrate had a negative effect on the matrix of the DFC. The matrix severely degraded after soaking, and no longer exhibited the same elastic behavior. As a result, the crack propagation did not behave identically to the specimens without compromised matrix material. Further investigation showed that there is sufficient density gradient between air and composite so the crack was well defined without the use of dye penetrate.

Once CT-scans were completed, the 3D image was exported as a serious of uint8 slices. These slices were reassembled in Matlab to visualize the internal damage. First, the images were loaded and converted to grey scale. The grey scale value assigned to each pixel is representative of the local density. To capture the desired information and eliminate excess

noise a filter with specific grey scale range was applied to the images. Then the images were cropped to contain just the crack front. This helps speed processing time when assembling the slices into a 3D image. Threshold values were applied to separate the air, zinc and composite. In the case without dye penetrate, only one threshold value was applied. The slices were then compiled into a 3D image.

The results of this process are shown for a size 2 and a size 3 specimen in Figure 3.14 and Figure 3.15 respectively. The specimens were tested to propagate the crack forward a preliminary amount. That initial crack front it visible in the image on the top. After the scan, the specimen was returned the load frame, and the crack was propagated a second time. This second crack front is visible in the image on the bottom. The load and displacement curve that occurs to propagate the crack between the two images are shown in 3.16. During image analysis, a grey scale value is assigned for the density throughout the material. In these images, the threshold value has been set so all that is visible is the very low density air. Locations that are light grey designate a single new surface, like delamination. The regions of increased darkness correlate to locations where there is more than one new surface, like fiber bridging or the presence of two cracks as a result of crack bifurcation.

Looking at the size 2 specimen in Figure 3.14, the image on the left contains small string like clusters of fibers are indicative of fiber bridging. Additionally, a full platelet can be easily visualized that has delaminated on both sides to bridge the two new surfaces. The right image shows a section of crack bifurcation. The crack splits and generates two surfaces, the reconnects and continues to propagate forward.

For the size 3 coupon, depicted in Figure 3.15, a sizable dark area appears on the scan that is characteristic of a crack bifurcation and long segment of parallel crack growth. This section is outlined for clarity. Note that the crack front in the scan on the bottom is much less full than the scan on the top. In Figure 3.16, the load and displacement plot shows that the crack growth is arrested very rapidly after initiation. It is reasonable that the sparsity of the crack front is representative of this behavior. The complex mesostructure causes different fracture toughness across the width of the specimen as a function of platelet orientation and method of crack propagation. The short drop could represent a small release of energy that only propagated a select portion of the crack front where the least amount of

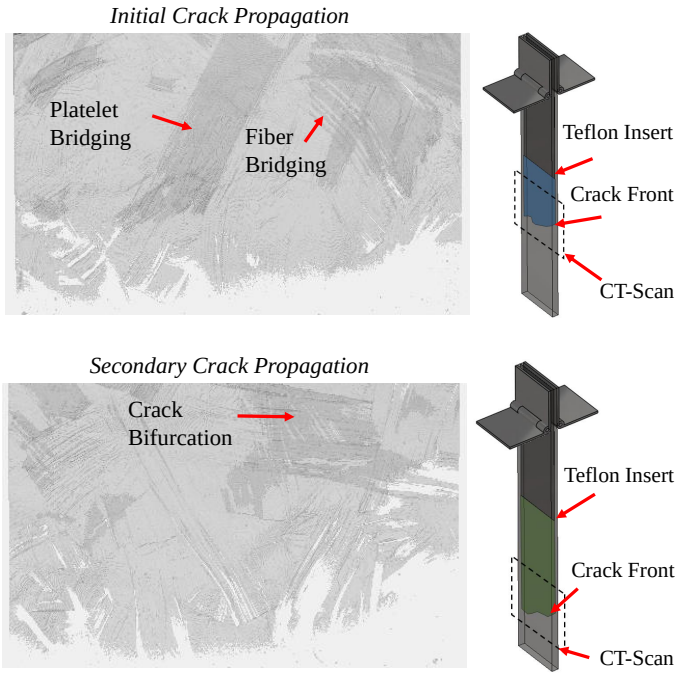

Figure 3.14: Size 2: CT-scans of crack front

energy was required to do so. Area that have a higher fracture toughness remain intact.

Notice that all of the crack fronts are non-linear and ragged. Platelet orientation variability, both in plane and out of plane, prevent the crack front from being linear. This provides insight to the limitations of traditional fracture energy calculations that assume a linear crack front and require crack length for prediction of fracture energy.

3.2.7 Buckling

The desired behavior for DCB test is for the crack to propagate through the center of the laminate to ensure equal bending of each arm and isolate the interlaminar fracture energy. Although this was achieved for most coupons, not all cracks propagated as anticipated. In some of the smallest specimens, size 1, the thickness of the arm was not sufficient to support the applied bending moment. This resulted in buckling of the arm, shown in Figure .

Figure 3.18 shows three different CT-scanned images of a buckled DFC coupon. The

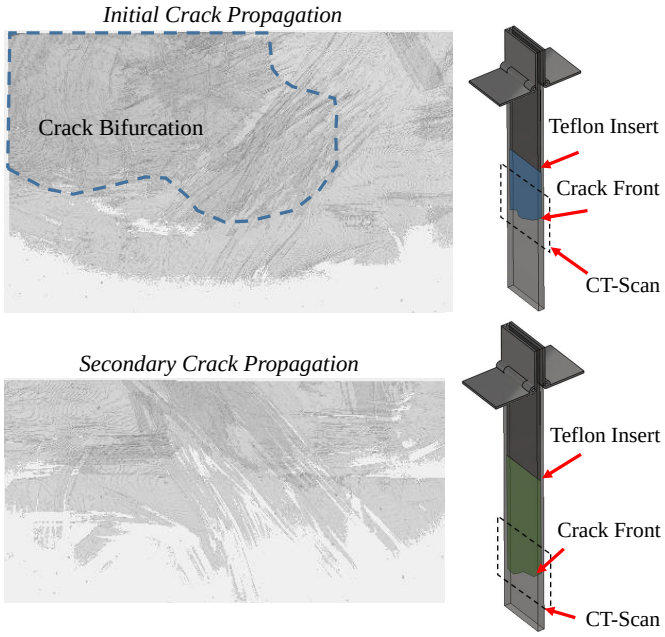

Figure 3.15: Size 3: CT-scans of crack front

left image is the crack before any loading has been applied. The crack diverges from peal ply and propagates away from the midplane of the coupon. The coupon is then tested with an Instron load frame. The center image shows the damage that occurred during the test. The right arm becomes insufficiently thick to support bending stresses and begins to buckle. Notice that the crack propagates forward a small amount and significant localized damage occurs on the right arm. The coupon is tested a second time, and the buckling continues. There is no forward crack propagation, only increased localized damage.

Figure 3.19 shows the 3D CT-Scan of the crack front. In the first image the crack has not been propagated. The texture in the image is indentations left by the Teflon insert that initiated the crack. The center image is of the specimen after it has been loaded initially, and the crack propagated forward a small amount. Localized damage from buckling is starting to appear on the right hand side of the image. The specimen is then loaded a second time and another image is captured with the CT-Scanner. The image on the right shows the final

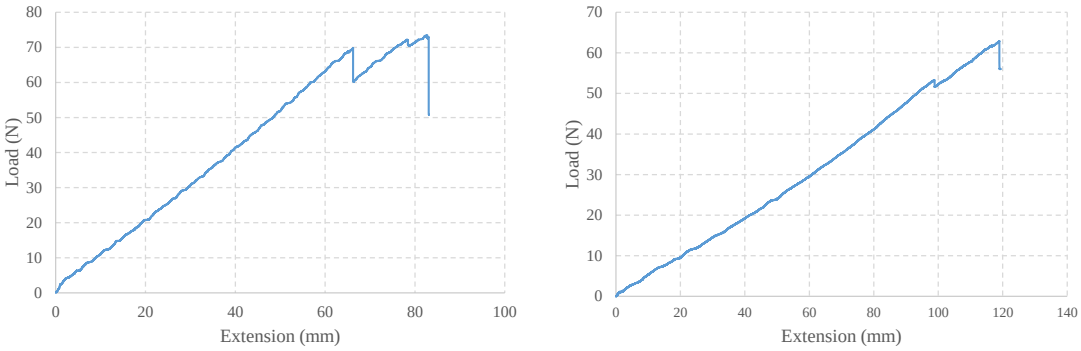

Figure 3.16: Load vs displacement curve *left*: Size 2, *right*: Size 3

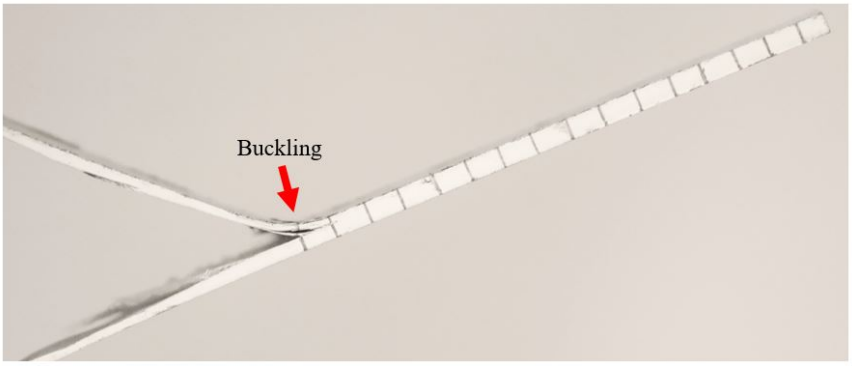

Figure 3.17: Buckling coupon - during DCB test

scan where the crack has not propagated forward. Instead, the increased density of localized damage appears as a darkened area in the CT-Scan.

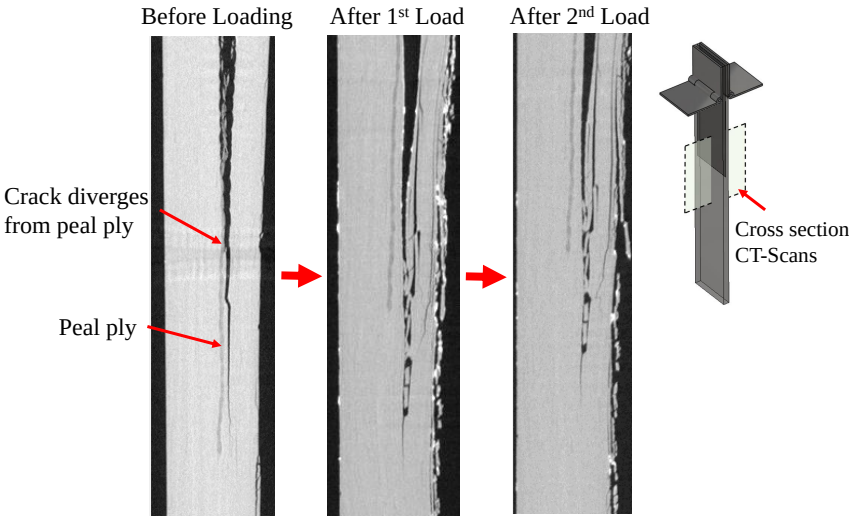

Figure 3.18: Buckling coupon - cross section of CT-scan

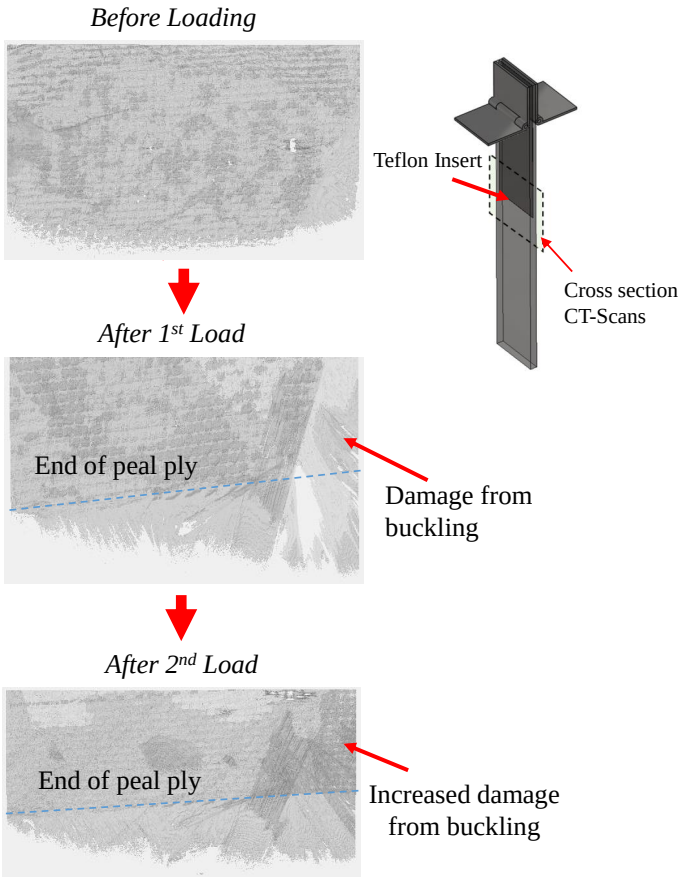

Figure 3.19: Buckling coupon - 3D CT-scan

Chapter 4

TEST RESULTS AND DISCUSSION

The following graph, Figure 4.1, contains all the data collected from the DCB tests. The size of the coupon increases from the smallest, size 1, to the largest, size 3. It is clear from this data that DFC does not follow traditional post peak behavior. The data exhibits a sawtooth pattern with multiple peaks through the duration of the test. Each drop in the load and displacement graph correlates to unstable crack propagation. After propagation, the crack is arrested by the complex mesostructured of the DFC, increased load is required to propagate the crack further. The peak loads per size have been averaged for each size of coupon, along with the standard deviation. The peak load increases with the size of the coupon, although there is some overlap between the load experienced by the size 2 and size 3 specimens.

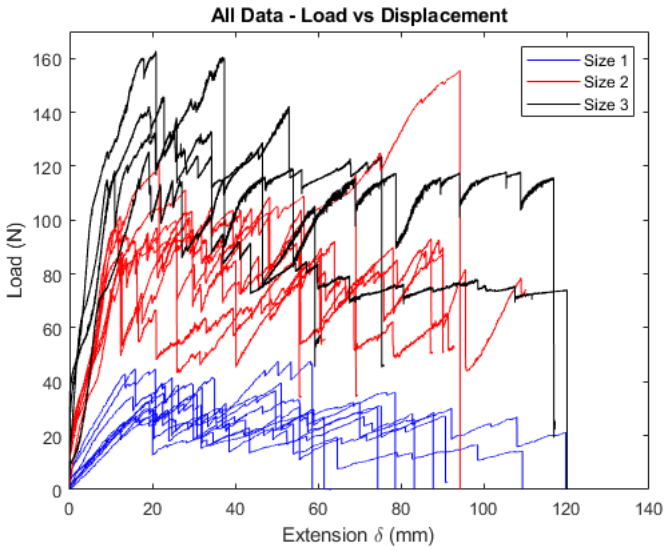

Figure 4.1: Load and displacement data for all DFC coupons

Size	Average Peak Load *(N)*	Standard Deviation
1	40.6	9.1
2	111.2	20.7
3	145.5	18.9

Table 4.1: Average peak load during DCB test per specimen size

For reference, Figure 4.2 contains a load and displacement curve for a traditional quasi-brittle material, such as a laminated composite, [45]. Notice that there is a single peak load followed by significant decrease in load required to propagate the crack forward.

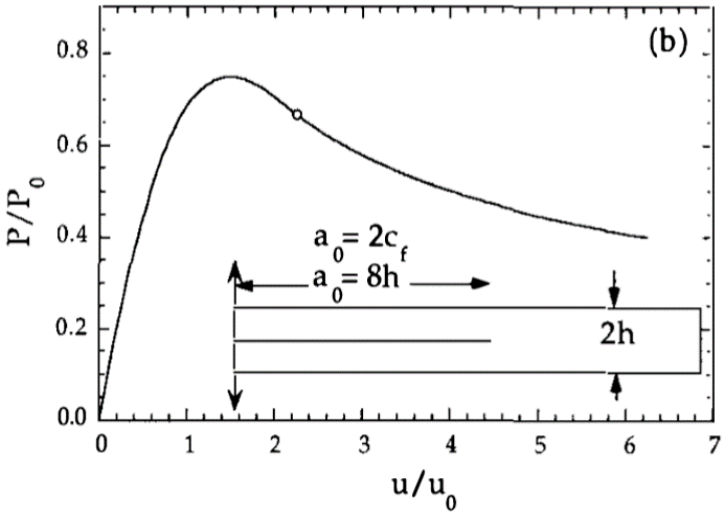

Figure 4.2: Typical load and displacement curve for quasi-brittle materials, [45]

4.1 Crack Bifurcation

Specimen 110 exemplifies the crack bifurcation damage mechanism. Figure 4.3 shows the load and displacement curve for the DCB test. There is a distinct sawtooth behavior associated with the peaks throughout the test. The top picture of Figure 4.3 shows the crack before the drop in the load displacement curve located at the red dot. In the bottom, pic-

ture of Specimen 110, the crack has propagated forward. The drop in the curve correlates to an unstable propagation of the crack. After the fifth drop, shown in Figure 4.4, there is a significant increase in load before the next distinct load drop. This is a consequence of the crack splitting into two in order to navigate around a transverse platelet with respect to the direction of crack propagation. The increased energy required to produce more new surface area is reflected in the load and extension data.

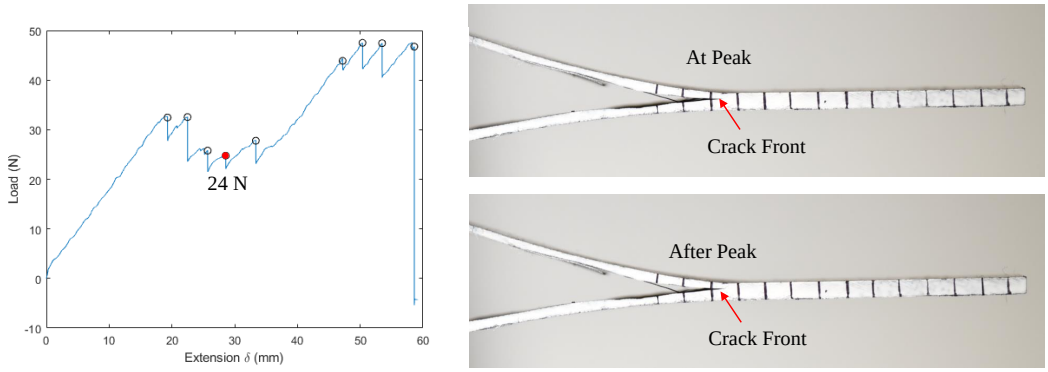

Figure 4.3: Specimen 110: DCB test with single crack front

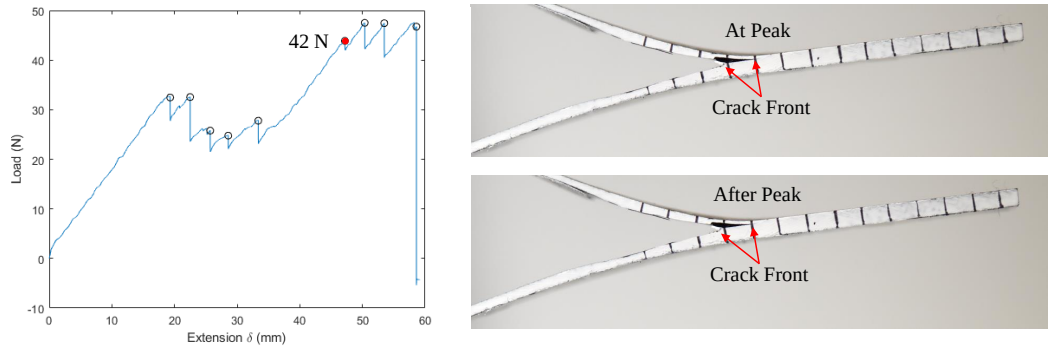

Figure 4.4: Specimen 110: DCB test initiation of secondary crack

4.2 Fiber Bridging

Figure 4.5 shows the load and displacement curve for a Size 3, largest sized, specimen. During fracture, this specimen had a large amount of fiber bridging. This is visibly evident in the Figure 4.5 and was audibly evident through a series of 'pings' throughout the test. The individual fibers were pulled in tension and could be heard breaking. Notice the slope of the load and displacement curve. Traditionally, quasi-brittle materials, like composites, have some strain softening before unstable crack propagation. This presents itself as a bending over of the load and displacement curve, similar to yielding, before the drop in load. In this case, the sawtooth peaks do not exhibit strain softening before crack propagation. This is a result of fiber bridging. When a fiber bridges between the two surfaces it loaded in tension. Instead of the matrix material that would traditionally resist the crack opening, the tension in the individual fibers are supporting the load. Because these fibers are brittle and break in tension, there is no strain softening. The load is increased until the fiber has reached its capacity, then it breaks, resulting in stiff peaks in the load and displacement graphs.

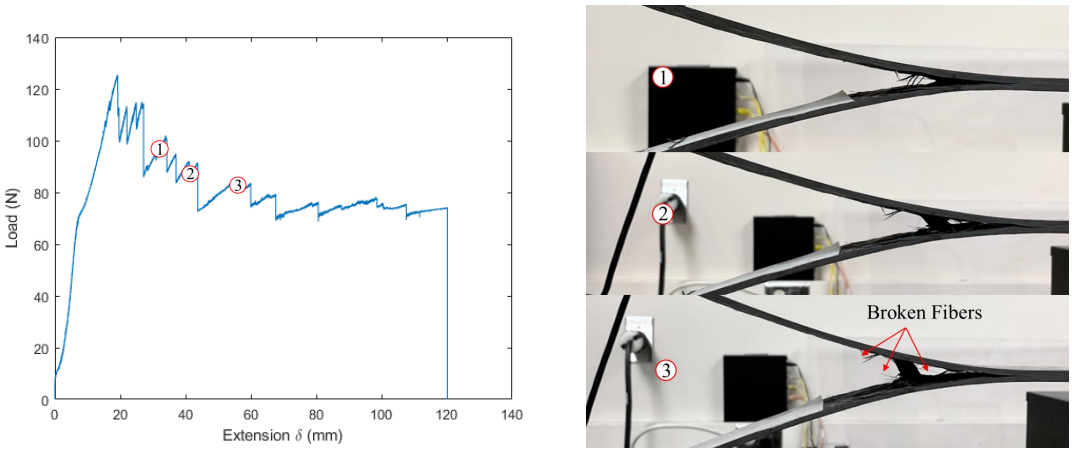

Figure 4.5: Specimen 308: brittle material behavior

4.3 Quasi-Brittle Behavior

A consequence of the complicated mesostructure of DFC is unique load and displacement curves and damage progression for each coupon. In opposition to the brittle peaks of Specimen 308, Specimen 306 has a significant amount of strain softening and exhibits definitively non-brittle behavior. These two coupons are the same size and were cut from the same sheet of DFC. The load and displacement curve of Specimen 306 is shown in Figure 4.6. Before each significant drop, the curve rounds over exhibiting definitively quasi-brittle behavior. This is a function of the micro damage in the fracture process zone ahead of the crack tip. The difference in behavior could be a result of fiber volume faction. It is possible that there is an uneven distribution of resin through the DFC laminate due to an uneven pressure distribution in the heated platen press.

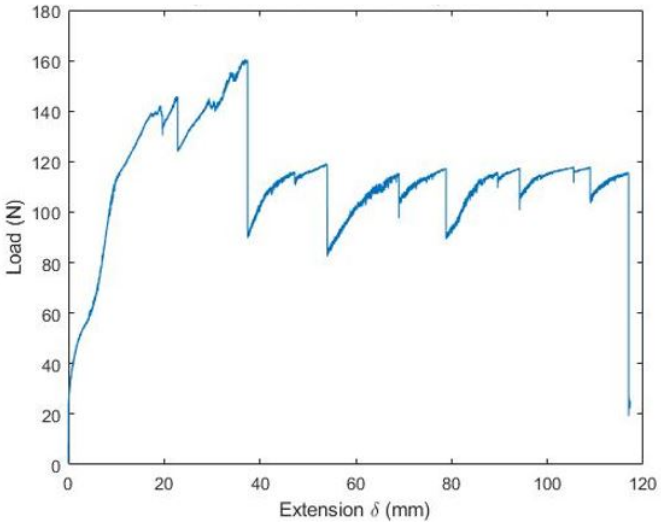

Figure 4.6: Specimen 306: quasi-brittle material behavior

4.4 Location of Peak Load

For traditional laminates, the largest stress usually occurs at first peak of the test, and post peak, the crack propagates with relative ease. In DFC, the first peak load is not necessarily the largest. Figure 4.7 shows the load and displacement curves for two size 1, the smallest, specimens. Both specimens are cut from the same sheet of DFC. Specimen 108, experiences

a peak load at the beginning of the test, and peaks progressively decrease in magnitude as the test continues. Conversely, the peak loads of Specimen 102 increase throughout the duration of the test. This shows that the energy required to propagate the test is not entirely a function of crack length, but also depends on the mesostructure of the DFC.

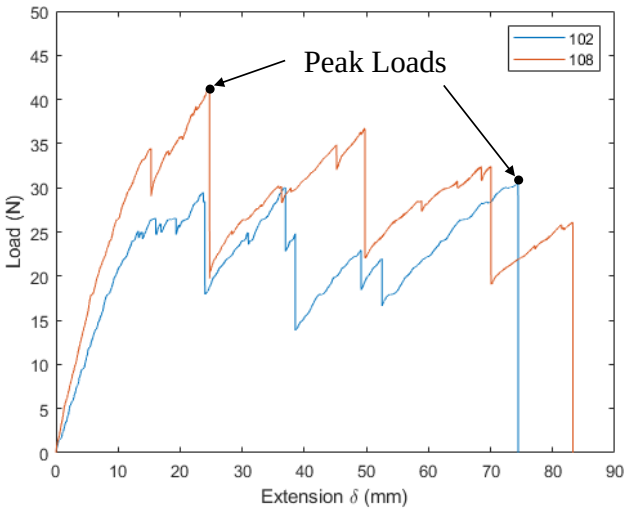

Figure 4.7: Specimens 102 and 108: load and displacement

Overall, the platelet geometry shows significant promise in arresting crack propagation. Complex mesostructure causes fiber bridging, and crack bifurcation which require additional energy to propagate the crack. Traditional laminated composites struggle with delamination in failure. DFC is less susceptible to this uninhibited crack propagation. However, the sporadic behavior of DFC makes fracture energy difficult to calculate and predict.

4.5 Fracture Energy

4.5.1 Methods

There are a number of methods that are used to calculate fracture energy. One method suggested by ASTM Standard D5528-13 is Modified Beam Theory. This says the that

fracture energy can be estimated as $G_I = \frac{3P\delta}{2ba}$. This expression uses beam theory for the strain energy release rate and assumes a perfectly built-in double cantilever beam at the delamination front. This fails to account for the rotation that occurs at the delamination front, the non-linearity of the delamination front, and the potential for multiple crack fronts. Since the crack does not necessarily propagate along the neutral axis, the thickness of the arms does not stay constant. This variability is uncapturable by beam theory. Additionally, the highly quasi-brittle behavior makes it difficult to accurately predict the location of the crack tip. This is true for all beam based energy prediction methods.

For quasi-brittle materials, like composites, it has been shown that the non-negligible fracture process zone can be accurately captured in the prediction of fracture energy by applying Bažant's Type II Size Effect Law [34, 45]. The purely energetic size effect, Type II, refers to structures with an existing notch or stress-free crack and can be written as:

$$\sigma_N = Bf_t'(1 + D/D_0)^{-1/2} \tag{4.1}$$

where $\sigma_N = P/bD$ or P/D^2 is the nominal strength for scaling in two or three dimensions; P is the maximum applied load, D is the characteristic length, b is the thickness, f_t is the material tensile strength, and B and D_0 are structural parameters. The Size Effect Law in terms of fracture characteristics is

$$\sigma_N = \sqrt{\frac{E'G_f}{g'(\alpha_0)c_f + g(\alpha_0)D}} \tag{4.2}$$

Where the structural parameters are expressed as

$$[D_0 = c_f \frac{g'(\alpha_0)}{g(\alpha_0)} \tag{4.3}$$

$$Bf_t' = \sqrt{\frac{E'G_f}{c_f g'(\alpha_0)}} \tag{4.4}$$

Where $\alpha_0 = a_0/D$ = relative crack length, c_f = effective length of FPZ, $g(\alpha) = D(bK_I/P)^2$ = dimensionless energy release rate, K_I = stress intensity factor, $g'(\alpha_0) = dg(\alpha)/d\alpha$ at $\alpha = \alpha_0$, $E' = E$ or $E/(1-\nu^2)$ for plane stress or plane strain respectively, ν = Poisson's ratio, E = Young's modulus, and G_f = fracture energy. G_f and c_f can be

calculated through a linear regression analysis of the experimental data by leveraging the following transformation. $Y = \frac{1}{\sigma_{NC}^2}$ and X = D. Plotting this results and linearly fitting the data results in a line

$$Y = Ax + B \tag{4.5}$$

$$A = \frac{g_0}{E'G_f} \tag{4.6}$$

$$B = \frac{c_f g_0'}{E'G_f} \tag{4.7}$$

This graph is shown in Figure 4.8. A and B can be found through a linear regression. Then G_f and c_f can be found by solving the above system of equations.

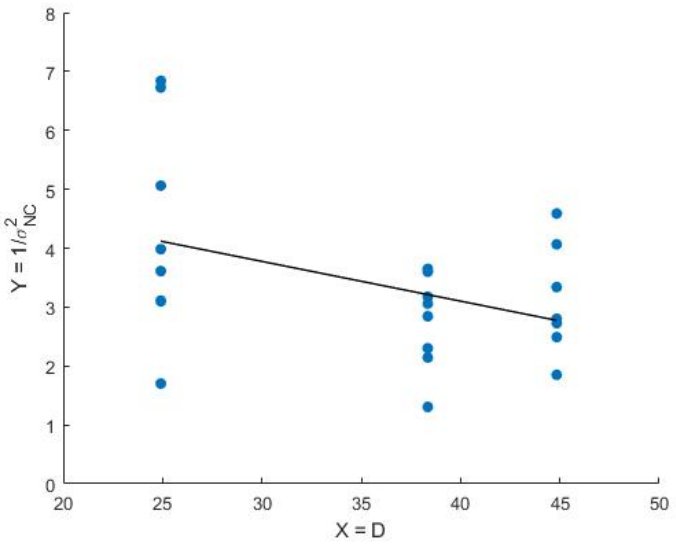

Figure 4.8: Linear regression for size effect calculations

Completing this calculation for the data collected for the DCB tests of DFC results in a negative fracture energy, G_f and a negative length of FPZ, c_f. This could be due to the significant scatter of data points, or the range in specimen size. However, it appears that homogenized framework on which SEL stands is not suitable to capture the complex

mesostructural phenomena underpinning the fracture behavior. For this, a mesoscale framework is necessary.

4.5.2 Calculations

The average fracture energy of each coupon was calculated with a graphical representation method described by Bažant, [49]. The load and extension data was used to find the energy require for fracture. The area under the entire curve is representative of the total work done to open the specimen. Assuming no residual plastic deformation, a line is drawn from the end of the last test point back to zero load and zero displacement. The area under this line correlates to the elastic energy required to open the specimen. Subtracting the elastic energy from the total work results in the energy supplied for fracture, see Figure 4.9 for visual representation. This is then divided by the new surface area to calculate the fracture energy. It is important to note that this is an approximation. The fracture energy is heavily dependent on the length of the crack. The nonlinearity of the crack front and the non-negligible fracture process zone, make the visual inspection of the crack front an estimation, not a precise measurement. The average fracture energy was calculated as:

$$G = \frac{EnergyForFracture}{2 * W * \Delta a} \tag{4.8}$$

Where G is the fracture energy, W is the width of the specimen and Δa is the change in crack length.

The average fracture energy calculated for each specimen size is shown in Table 4.2.

Size	Average Fracture Energy (N/mm)
1	0.54
2	0.60
3	0.80

Table 4.2: Average apparent fracture energy for each size investigated

As discussed earlier, the fracture process zone is a nonlinear area ahead of the crack

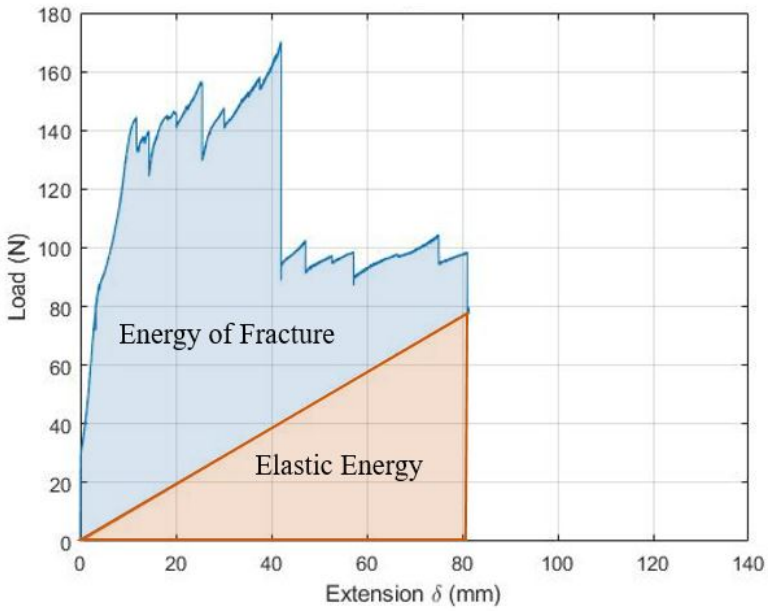

Figure 4.9: Graphical representation of energy calculation

tip that contains significant micro damage leading to local material softening. At crack initiation the FPZ is relatively small, and increases in size as the crack grows in length until it reaches a fully developed equilibrium size. The size of the fully developed FPZ is a function of material and part geometry. The fracture energy of a material increases with the crack length until the FPZ is fully developed. At this point the fracture energy stabilizes and the crack propagates self similarly. This is commonly communicated in the form of an R-curve. The specimens tested in this research are not large enough for the FPZ to fully develop. More coupons, of increasing size, would need to be tested until a plateau is reached to quantify the full capabilities of DFCs. In the framework of designing with DFC, it is important to note that sufficiently small parts will not experience that same benefits of increased fracture energy due to complex internal geometry. Energy is dissipated through micro damage in the FPZ, so an underdeveloped of the FPZ experiences less energy dissipation and consequently lower fracture energy.

Although the majority of the specimens have fracture energies clustered around an average, there are some significant outliers. For the Size 2 coupons, the average fracture energy

is 0.60 N/mm. However, one of the coupons has a fracture energy of 1.08 N/mm, which is 69.5% increase compared the average. The graph in Figure 4.10 shows the load and extension curve for this coupon. The complex internal architecture of DFC leads to a variety fracture behaviors, and in this case has allowed the coupon to support a considerably increased load before failure.

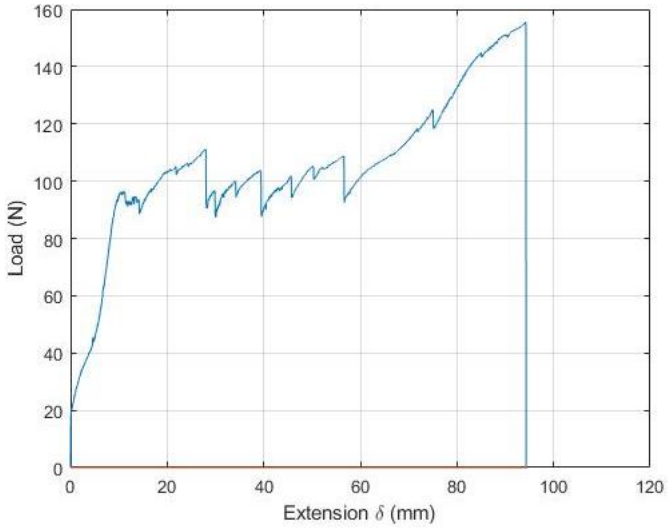

Figure 4.10: Specimen 207: load and displacement

Investigation of other research containing DCB tests that capture the Mode I fracture energy of carbon fiber and epoxy laminates show a range of 0.21 N/mm to 0.46 N/mm, [50, 51]. Kumar *et al.* studied Mode I toughness enhancement using nanographene on unidirectional carbon fiber composites [50]. DCB specimens were manufactured per ASTM D5528 with varying levels of nanographene. The control coupons, those containing no nanographene, are reported to have a fracture toughness between 0.369 N/mm and 0.458 N/mm. Low *et al.* conducted a study on unidirectional carbon fiber and epoxy laminates where the displacement rate was varied, [51]. The results, shown in Figure 4.11, show a Mode I fracture toughness between 0.21 N/mm and 0.30 N/mm [51]. The figure shows a comparison of data

reduction schemes including Classical beam theory (CBT), Modified beam theory (MBT), Compliance calibration (CC), and Modified Compliance calibration (MCC).

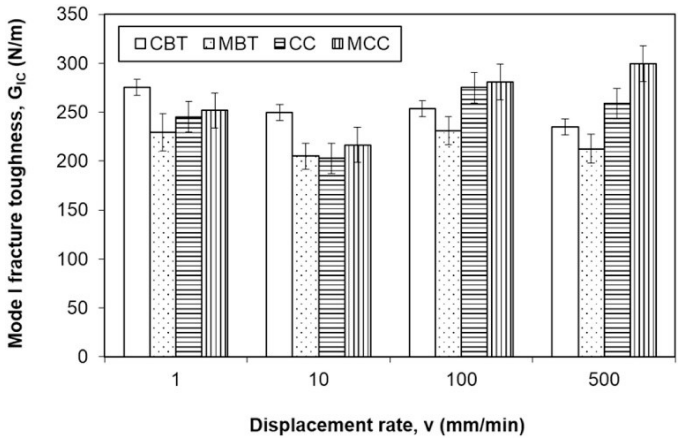

Figure 4.11: Comparison of the Mode I fracture toughness, [51]

Chapter 5

CONCLUSION

Mode I fracture behavior of discontinuous fiber composites is studied for three sizes of coupons. The damage that occurred was visualized through optical microscope, visual inspection, and micro-CT scans. Damage mechanisms are characterized and common damage progressions are identified.

- Micro damage in DFC specimens includes, delamination, matrix cracking, and fiber breaking.

- Damage mechanisms that contribute to fracture energy are delamination, fiber nesting, fiber bridging, crack bifurcation

- These damage mechanisms commonly occur in progressions. Fiber nesting leads to fiber bridging which, if that crack is met by a platelet transverse to its direction of propagation, can result in crack bifurcation. Fiber bridging can also result in fiber breaking if the strength of the fiber is not sufficient to transfer the load.

- Complex platelet architecture is responsible for the multitude of types of damage, and the ability to arrest unstable crack growth.

- Load and displacement plots depict a sawtooth shape that reflects the pattern of crack propagation followed by the stop of extension due to internal geometry.

- The fracture energy is calculated using an area method and ranges from 0.54 to 0.80 N/mm for the smallest and largest specimens respectively. This is 80%-167% higher than reported values for unidirectional carbon fiber epoxy laminates.

- The continuing increase of fracture energy suggests that the fracture process zone in these coupons is not fully developed.

- Testing larger specimens will reveal the full capacity of the material.

Overall, discontinuous fiber composites show great promise for use in industry. This study has shown that they have an increased fracture energy and the capacity to stop crack propagation, where as traditional composite parts usually fail in delamination. Their complex mesostructure make them ideal for three dimensional parts with out of plane loads because platelets are not in a two dimensional plane, the have out of plane orientation as well. This, along with the improved production times and recyclable nature make DFCs an excellent candidate for complex and cutting edge part design.

Bibliography

[1] M. Benevento W. Seneviratine R. Liang E. Witten S. Mazumdar, D. Pichler. 2020 state of the industry report. *American Composites Manufacturers Association*, 2020.

[2] B. Esp. *Practical Analysis of Aircraft Composites*. Grand Oak Publishing, 2017. ISBN 9780983245391.

[3] G.S. Springer L.P. Kollár. *Mechanics of Composite Structures*. Cambridge University Press, 2009. ISBN 9780521126908.

[4] J. Takahashi Y. Wan. Tensile and compressive properties of chopped carbon fiber tapes reinforced thermoplastics with different fiber lengths and molding pressures. *Composites Part A: Applied Science and Manufacturing*, 87:271–281, 2016.

[5] F. Ohlsson L.E. Asp S. Pimenta M. Alves, D. Carlstedt. Ultra-strong and stiff randomly-oriented discontinuous composites: Closing the gap to quasi-isotropic continuous-fibre laminates. *Composites Part A: Applied Science and Manufacturing*, 132, 2020.

[6] A. Jain C. González J. LLorca S. Nutt B.C. Jin, X. Li. Optimization of microstructures and mechanical properties of composite oriented strand board from reused prepreg. *Composite Structures*, 174:389–398, 2017.

[7] M. Yari. Galvanic corrosion of metals connected to carbon fiber reinforced polymers. 2017.

[8] J. Slone. Composites recycling becomes a necessity. *Composite World*, 2012.

[9] S. Nutt G. Nilakantan. Reuse and upcycling of thermoset prepreg scrap: Case study with out-of-autoclave carbon fiber/epoxy prepreg. *Journal of Composite Materials*, 52: 341–360, 2017.

[10] P. McMullen. Fibre/resin composites for aircraft primary structures: a short history, 1936-1984. *Composites*, 15, 1984.

[11] S. Douglass J. Yang M.E.Tuttle M. Salviato S. Ko, J. Davey. Effect of the thickness on the fracturing behavior of discontinuous fiber composite structures. *Composites Part A: Applied Science and Manufacturing*, 125, 2019.

[12] M. E.Tuttle M. Salviato S. Ko, J. Yang. Effect of the platelet size on the fracturing behavior and size effect of discontinuous fiber composite structures. *Composite Structures*, 227, 2019.

[13] D. Brosius. Boeing 787 update. 2007.

[14] Hexcel. Airbus delivers first a350-1000. *Reinforced Plastics*, 62:109, 2018.

[15] S. Black. Redesigning for simplicity: Military oem makes the switch from sandwich construction to compression. *High-Performance Composites Magazine*, 2012.

[16] Lamborghihi. Technical data sheet: Forged composites, 2012. URL `https://www.lamborghini.com/en-en/brand/innovation-excellence/forged-composites`.

[17] B. Wade P. Feraboli, F. Gasco. Lamborghini "forged composite®" technology for the suspension arms of the sesto elemento. 2012.

[18] Volkswagen Group. Volkswagen group lamborghini wins the innovation award at the jec composites 2016, 2016. URL `www.volkswagenag.com`.

[19] Pur Carbon. What is forged carbon and where did it come from, 2018. URL `www.pur-carbon.com`.

[20] Callaway Golf Company. Callaway golf introduces new diablo octane drivers fairway woods, 2010. URL `www.callawaygolf.com`.

[21] Golf News Now. Callaway launches razr. 2011.

[22] L. Lessard A. Yousefpour M. Selezneva, S. Roy. Analytical model for prediction of strength and fracture paths characteristic to randomly oriented strand (ros) composites. *Composites Part B: Engineering*, 96:103–111, 2016.

[23] B.R. Denos W.B. Avery R.B. Pipes S.G. Kravchenko, D.E. Sommer. Structure-property relationship for a prepreg platelet molded composite with engineered meso-morphology. *Composite Structures*, 210:430–445, 2019.

[24] B.R. Denos W.B. Avery R.B. Pipe S.G. Kravchenko, D.E. Sommer. Tensile properties of a stochastic prepreg platelet molded composite. *Composites Part A: Applied Science and Manufacturing*, 124, 2019.

[25] S. Mahadzir S.Z.H.Shah, R.S. Choudhry. A new approach for strength and stiffness prediction of discontinuous fibre reinforced composites (dfc). *Composites Part B: Engineering*, 183, 2020.

[26] S.G. Kravchenko. Failure analysis in platelet molded composites. 2017.

[27] J.M. Robinson I.M. Robinson. The effect of fibre aspect ratio on the stiffness of discontinuous fibre-reinforced composites. *Composites*, Volume 25:499–503, 1994.

[28] K. Hayakaw T. Yamamoto. Evaluation of mechanical properties of randomly compression molded carbon fiber reinforced thermoplastic sheet made of unidirectional tape. *Procedia Manufacturing*, 125:1708–1715, 2018.

[29] Y. Zhang B. Spitzlei I. Ohsawa J.Takahashi Q. Guo, B. Xiao. Numerical and experimental study of the mode i interlaminar failure of chopped carbon fiber tape reinforced thermoplastics. *21st International Conference on Composite Materials*, 2017.

[30] Z. Yousa f N.T.Vo T. Lowe P. Potluri P.J.Withers Y. Chai, Y.Wang. Damage evolution in braided composite tubes under torsion studied by in-situ x-ray computed tomography. *Composites Science and Technology*, 188, 2020.

[31] D. Coker B.O. Yavuz, L. Parnas. Interlaminar tensile strength of different angle-ply cfrp composites. *Procedia Structural Integrity*, 21:198–205, 2019.

[32] R. Hawkins R. Jayaram C. Lynch R. El Mamoune M. Nguyen N. Pekhotin N. Stokes D.N. Wu M.E. Tuttle J. Yang M. Salviato S. Ko, K. Chan. Characterization and computational modeling of the fracturing behavior in discontinuous fiber composite structures. *Society for the Advancement of Material and Process Engineering – North America*, 2018.

[33] M. Salviato, K. Kirane, S.E. Ashari, Z.P. Bažant, and G. Cusatis. Experimental and numerical investigation of intra-laminar energy dissipation and size effect in two-dimensional textile composites. *Composites Science and Technology*, 135:67–75, 2016.

[34] M. Salviato, K. Kirane, Z.P. Bažant, and G. Cusatis. Mode I and II interlaminar fracture in laminated composites: a size effect study. *Journal of Applied Mechanics*, 86 (9), 2019.

[35] M. Salviato, S.E. Ashari, and G. Cusatis. Spectral stiffness microplane model for damage and fracture of textile composites. *Composite Structures*, 137:170–184, 2016.

[36] M. Salviato, V.T. Chau, W. Li, Z.P. Bažant, and G. Cusatis. Direct testing of gradual postpeak softening of fracture specimens of fiber composites stabilized by enhanced grip stiffness and mass. *Journal of Applied Mechanics*, 83(11), 2016.

[37] K. Kirane, M. Salviato, and Z.P. Bažant. Microplane-triad model for elastic and fracturing behavior of woven composites. *Journal of Applied Mechanics*, 83(4), 2016.

[38] K. Kirane, M. Salviato, and Z.P. Bažant. Microplane triad model for simple and accurate prediction of orthotropic elastic constants of woven fabric composites. *Journal of Composite Materials*, 50(9):1247–1260, 2016.

[39] M. Salviato, K. Kirane, and Z.P. Bažant. Statistical distribution and size effect of residual strength of quasibrittle materials after a period of constant load. *Journal of the Mechanics and Physics of Solids*, 64:440–454, 2014.

[40] C.H. Mefford, Y. Qiao, and M. Salviato. Failure behavior and scaling of graphene nanocomposites. *Composite Structures*, 176:961–972, 2017.

[41] Y. Qiao and M. Salviato. Strength and cohesive behavior of thermoset polymers at the microscale: A size-effect study. *Engineering Fracture Mechanics*, 213:100–117, 2019.

[42] C. Carloni, G. Cusatis, M. Salviato, J.L. Le, C.G. Hoover, and Z.P. Bažant. Critical comparison of the boundary effect model with cohesive crack model and size effect law. *Engineering Fracture Mechanics*, 215:193–210, 2019.

[43] Y. Qiao and M. Salviato. Study of the fracturing behavior of thermoset polymer nanocomposites via cohesive zone modeling. *Composite Structures*, 220:127–147, 2019.

[44] Marco M. Salviato and Z.P. Bažant. The asymptotic stochastic strength of bundles of elements exhibiting general stress–strain laws. *Probabilistic Engineering Mechanics*, 36: 1–7, 2014.

[45] Z. Li Z.P. Bažant, I.M. Daniel. Size effect and fracture characteristics of composite laminates. *J Eng Mater-T ASME*, 118(3):317–24, 1996.

[46] P.D. Mangalgiri W.S. Johnson. Investigation of fiber bridging in double cantilever beam specimens. *Journal of Composites Technology Research*, 9(1):pp. 10–13, 1987.

[47] J.P. Lucas. Delamination fracture: Effect of fiber orientation of a continuous fiber composite laminate. *Engineering Fracture Mechanics*, 42(3):543–561, 1992.

[48] M. Konig J. Andersons. Dependence of fracture toughness of composite laminates on interface ply orientations and delamination growth direction. *Composite Science Technology*, 64:2139–2152, 2004.

[49] J. Planas Z.P. Bažant. *Fracture and Size Effect in Concrete and Other Quasibrittle Materials*. CRC Press LLC, 1997. ISBN 084938284X.

[50] S. Roy A. Kumar. Characterization of mixed mode fracture properties of nanographene reinforced epoxy and mode i delamination of its carbon fiber composite. *Composites Part B: Engineering*, 134, 09 2017.

[51] M. Johar H.A. Israr K.J. Wong K.O. Low, S.M. Teng. Mode i delamination behaviour of carbon/epoxy composite at different displacement rates. *Composites Part B: Engineering*, 176, 2019.